Review

Emerging applications of stimulated Raman scattering microscopy in materials science

Qian Cheng,[1,3] Yupeng Miao,[2,3] Joseph Wild,[1] Wei Min,[2,*] and Yuan Yang[1,4,*]

SUMMARY

Stimulated Raman scattering (SRS) is a nonlinear Raman scattering process that can amplify Raman scattering by up to 10^8 times under modern microscopy configuration. SRS microscopy has emerged as a powerful chemical imaging technique due to its high chemical, spatial, and temporal resolution. While SRS microscopy was originally designed for biomedical applications, it has drawn increasingly more attention from the materials science community in recent years. The high-speed and high-chemical sensitivity of SRS are attractive for both high-throughput material characterizations and capturing transient dynamics in chemical transport and reactions. It has been explored in various topics, such as 2D materials, energy storage and conversion, and polymerizations with great success. In this review, we discuss principles, instrumentation, and current applications of SRS microscopy in materials science, followed by our perspectives on future exciting topics to be studied by SRS microscopy.

INTRODUCTION

Imaging plays an important role in materials science as it provides rich information on spatial variation and temporal dynamics of material compositions, structures, and properties. The history of material imaging dates back to the invention of optical microscopy by Cornelis Drebbel in 1619.[1] In the last century, imaging tools have been quickly developed and significantly expanded our vision and understanding of materials. These instruments include but are not limited to optical microscopies (e.g., optical microscopy, polarization microscopy, near-field scanning optical microscopy, X-ray imaging),[2–5] vibrational microscopies (e.g., Fourier transform infrared microscopy, Raman microscopy),[6,7] electron microscopies (e.g., transmission electron microscopy),[8,9] scanning probe microscopies (e.g., scanning tunneling microscopy, atomic force microscopy [AFM]),[10,11] mass spectrometry-based imaging (e.g., time of flight-secondary ion mass spectroscopy),[12] and magnetic resonance imaging (MRI).[13] They probe material structures and compositions at different scales in time and space (Figure 1A). Among these imaging instruments, Raman microscopy is a powerful tool since it unveils critical information on the vibration of chemical bonds, a fundamental interaction in materials. Therefore, Raman microscopy has been widely used to visualize spatial and temporal evolution of a broad spectrum of materials, such as polymers,[14] ceramics,[15] 2D materials,[16] and biomaterials.[17] The information gained from Raman microscopies has not only transformed fundamental knowledge in materials science but also shed light on designing principles for materials engineering.

The most common Raman microscopy in materials science is spontaneous Raman microscopy, where a single laser beam shines onto a sample and the scattered light

Progress and potential

The conventional spontaneous Raman microscopy is a powerful tool that images chemical bonds in materials, but it suffers from the intrinsically weak Raman cross-sections and requires long acquisition time. As an emerging imaging tool, stimulated Raman scattering (SRS) microscopy significantly amplifies the Raman scattering signal. It has higher chemical sensitivity, faster imaging speed, and fine spatial resolution. Meanwhile, it is label-free and capable of 3D imaging. With its fast speed and superb chemical sensitivity, it can visualize the dynamic process in materials science, such as ion transport. SRS microscopy was originally invented for biomedical studies so it is not well known by the materials science community yet. In this review paper, we introduce the principle and instrumentation of SRS microscopy, applications in materials science, and discuss future potentials and challenges. We believe that SRS microscopy will become a valuable instrument for materials science.
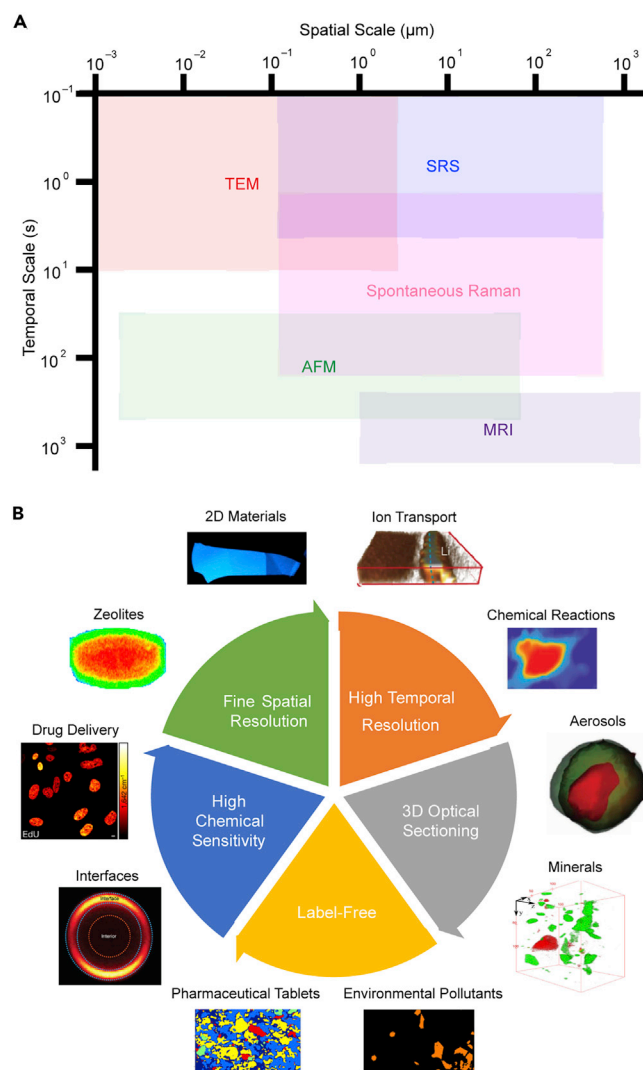
Figure 1. The resolution and application of SRS microscopy

(A) Typical spatial and temporal scales of common imaging techniques, including transmission electron microscopy, spontaneous Raman, SRS, MRI, and AFM. SRS microscopy has advantages in imaging speed and chemical sensitivity than the conventional spontaneous Raman microscopy.

(B) Key characteristics of SRS microscopy and its applications in materials science, including imaging the structure and the composition of aerosols,[18] minerals,[19] zeolites,[20] and 2D materials,[21] tracing ion transport,[22] drug delivery,[23] interface phenomena,[24] and polymerization,[25] and identifying the composition of pharmaceutical tablets[26] and environmental samples.[27]

is collected to acquire the Raman scattering information. A major challenge in such spontaneous Raman microscopy is its long accumulation time and low chemical sensitivity since the Raman scattering is an intrinsically weak process.[28] It typically requires an acquisition time of 1–10 s for a single pixel, and thus minutes, even hours for 2D and 3D imaging (Figure 1A). To address this issue, surface-enhanced Raman scattering (SERS) and tip-enhanced Raman scattering (TERS) have been developed by altering the local electric field with surface plasmons that can amplify the Raman signal by $\sim 10^4$–10^{10} times to the single-molecule level.[29] The enhanced signals remarkably improve the capability of Raman microscopy to detect weak signals and distinguish interfacial phenomena from bulk processes. However, the requirement of a metallic substrate in SERS and TERS significantly limits their scope of

[1]Program of Materials Science and Engineering, Department of Applied Physics and Applied Mathematics, Columbia University, New York, NY 10027, USA

[2]Department of Chemistry, Columbia University, New York, NY 10027, USA

[3]These authors contributed equally

[4]Lead contact

*Correspondence:
wm2256@columbia.edu (W.M.),
yy2664@columbia.edu (Y.Y.)
https://doi.org/10.1016/j.matt.2021.02.013

application; therefore, it is difficult to realize volumetric imaging by SERS/TERS. The substrate also needs to be compatible with the target material system, limiting applicable scenarios of this strategy.

Stimulated Raman scattering (SRS) is a substrate-free Raman process with a high degree of coherent signal amplification. It was first adapted into the microscope for biomedical studies in 2008, with both simultaneous signal amplification and volumetric imaging.[23,28,30,31] With a much higher Raman signal, SRS microscopy can reach a temporal resolution of ~1 μs/pixel, a spatial resolution of ~100 nm, a chemical sensitivity of ~1 μM, and automatic 3D optical sectioning (Figure 1A).[32] SRS does not require fluorescent dyes as in prevailing fluorescence imaging techniques. Such alien dyes are particularly difficult for labeling small molecules (e.g., glucose) and they often perturb the normal functions of small molecules.[33] Therefore, the non-invasive nature of SRS microscopy empowers it to be a versatile tool in biomedical imaging. For example, deuterium-labeled water has been used to monitor the global metabolic activities at the cell, tissue, and animal levels.[34] d_7-Glucose and alkyne-labeled glucose were applied to trace both the uptake and incorporation processes in live cells.[35–37] SRS imaging of deuterated fatty acids were used to track the different fates of saturated and unsaturated fatty acids, revealing their different spatial distribution and cell toxicity.[38] Also, SRS has been used to study bacterial biofilms, where significant metabolic heterogeneity was visualized.[39,40] A comprehensive summary of the biomedical applications of SRS microscopy can be found elsewhere.[32]

To the best of our knowledge, the application of SRS microscopy in materials science was not explored until 2017, 9 years after its birth. SRS microscopy is particularly attractive for accumulating high-volume and high-dimensional data of material structures for quantitative analysis, statistics, and even data-driven research, and understanding the complex temporal/spatial evolution of material systems (e.g., tracing chemical transport and chemical reaction). Since the first paper on observing molecular orientation in zeolite in 2018,[41] SRS microscopy has been applied to a wide range of systems in materials science (Figure 1B), such as 2D materials,[21,42] zeolites,[20] aerosols,[18] catalysis,[43] interfacial structures,[44] pharmaceutical materials,[45] and dynamic chemical reactions.[22,25] For example, Cheng et al.[22] demonstrated the visualization of ion depletion in battery electrolytes and its correlation with lithium dendrite growth. Li et al.[25] unveiled the initiation and propagation of polymerization of acrylamide. Nevertheless, this tool is not well known by the materials science community yet. In this review, we first introduce the working principle of this emerging SRS microscopy and recent progress in instrumentation, followed by applications in various material systems. Finally, perspectives on future opportunities and challenges of SRS microscopy for materials science are discussed.

WORKING PRINCIPLES AND INSTRUMENTATION OF SRS MICROSCOPY

Working principles

Vibrational spectroscopies, such as spontaneous Raman scattering spectroscopy, have long served as key measures for material characterizations.[46–48] Conventional spontaneous Raman spectroscopy uses one single laser (ω_p) shining onto the sample (Figure 2A). At the molecular level, all Raman scattering events involve the inelastic interactions between photons and molecules, which result in a photon energy change of either a loss (Stokes) or gain (anti-Stokes). By collecting the scattered photons, the vibrational signatures and concentrations of chemical bonds are acquired. This information is different from other characterization methods, such as crystallography (coordinates of
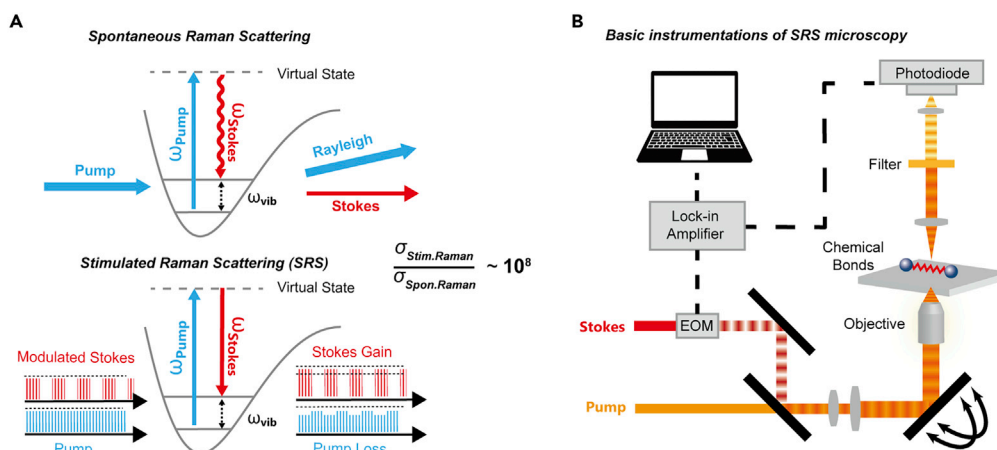
Figure 2. Fundamental principles and schematic of the SRS microscopy

(A) Comparison of conventional spontaneous Raman scattering (top) and stimulated Raman scattering (bottom) through molecular interaction. The addition of a Stokes beam dramatically enhances the vibrational transition rate by a factor of up to 10^8.

(B) The typical instrumentation of an SRS microscope. A pulsed pump beam is spatially and temporally synchronized with a modulated Stokes beam. After interaction with the specimen, the Stokes gain signal is filtered off while the pump loss signal is detected by a photodiode and amplified by a lock-in amplifier. The demodulated signal is digitized into pixel intensity.

specific atoms), UV-vis spectroscopy (energy differences between molecular orbitals), or mass spectroscopy (mass of entire molecules or fragments). This feature endows the vibrational Raman spectroscopy with high chemical specificity and provides rich bonding and structural information. Raman is less sensitive to polar bonds, hence it is more tolerant to a water background compared with infrared (IR) microscopy.[49] Moreover, the irradiation source of Raman is typically in the range of UV to near-infrared (NIR), so that the spectroscopy can be readily coupled with microscopy, which is highly favored for material studies. For years, technical advances have been made to extensively apply various Raman microscopies for material studies. For example, spontaneous Raman is widely used to determine the layer of graphene by examining its D and G peaks.[16] However, spontaneous Raman was known to have relatively low chemical sensitivity. In typical practice, spontaneous Raman spectroscopy requires a few seconds to obtain the spectrum at a single spot, so Raman mapping can take minutes to hours. To address the sensitivity issue, resonant Raman scattering techniques were also exploited to enhance the weak Raman signal by coupling electronic and vibrational motions of chromophores.[50,51]

SRS differs in many ways from the abovementioned Raman scattering phenomena.[28] It utilizes one extra laser beam (ω_s, Stokes beam) that is spatially and temporally synchronized with the pump beam (ω_p) to stimulate the vibrational transition rate and greatly promote the scattering cross-section (σ_{Raman}) by roughly 10^8 (Figure 2A). When the ground-state molecule is excited to the virtual state by a pump photon, the Stokes beam dramatically accelerates its relaxation process to the vibrational excited state as the energy difference between pump and Stokes photons matches the vibrational energy gap. During this transition event, a pump photon is consumed while a new Stokes photon is emitted. This results in a net loss of pump intensity and a gain of Stokes intensity. By modulating the pump or Stokes beam, the gain or loss can be detected by a high-frequency (~MHz) lock-in amplifier. The signal size of SRS can be interpreted from the stimulated Raman loss, typically proportional to $N_s \times \sigma_{Raman} \times I_p \times I_s$, where N_s is the number of target bonds, I_p and I_s are the intensity of pump and Stokes beams, respectively. As a consequence of the strong quantum amplification, the chemical sensitivity of SRS is much higher than that of spontaneous

Raman. The spatial resolution of SRS microscopy, on the other hand, is similar to conventional Raman microscopy, since they are both diffraction limited. It is worth noting that the standard SRS setup (Figure 2) with a picosecond laser pulse train only records the information of one wavenumber ($\omega_p - \omega_s$) at a time. It sacrifices multiple-channel information to acquire a much high temporal and chemical resolution. Therefore, SRS microscopy has great advantages when high temporal resolution and chemical sensitivity are required, such as studying the ion diffusion process. Spontaneous Raman microscopy should be chosen when spectrometric information on each spot is needed, such as distinguishing multiple species simultaneously.

Compared with other nonlinear Raman scattering processes, SRS has many unique advantages. Firstly, SRS is background free, as it directly probes the energy exchange between the laser field and chemical bonds. Secondly, compared with other coherent Raman scattering microscopies, such as coherent anti-Stokes Raman scattering, the SRS signal is free from the non-resonant background and is usually proportional to the concentration of chemical bonds if the peak position does not shift with varied concentration. This greatly simplifies data interpretation and facilitates quantification.[28] Thirdly, unlike SERS where the sample must be adsorbed by metal surfaces, SRS does not require any substrates. The enhancement factors from the SERS effect vary substantially, making it less applicable for imaging. In comparison, SRS can faithfully interrogate the spectral details while showing great linear concentration dependence as a far-field effect.[22,32] These features make SRS suitable for materials studies, and allow us to track the dynamic variation of chemical concentration in a rapidly changing environment.

Basic instrumentation of SRS microscopy

As the SRS stimulation requires an extra light source with a distinct wavelength, an SRS microscope is typically equipped with two laser sources: the initial incident beam for excitation (pump) and the stimulating beam (Stokes). The frequency difference ($\omega_p - \omega_s$) between the two beams matches exactly with the energy of specific vibrational modes of interest (Figure 2B). For full-spectrum measurement, it is obvious that the energy difference between the two lasers needs to be tuned. The typical SRS setup uses an optical parametric oscillator (OPO) to achieve wavelength sweeping. Moreover, the two beams are spatially and temporally synchronized before being guided into the microscope to achieve optimal synergy. Temporally, both beams are pulsed lasers to maximize the peak power, due to the nonlinear nature of stimulated scattering. Spatially, a confocal laser scanning microscope is needed to tightly focus the laser beams on a sample. Notably, although the scattering cross-sections are greatly enhanced via stimulated scattering, the relative intensity changes (pump loss and Stokes gain) are still small compared with the intensities of incident beams (e.g., $\sim 10^{-4}$ of the incident beams). To extract the relatively weak scattering signal, either the pump or Stokes beam is modulated by an electro-optic modulator, so that the pump loss or Stokes gain signal can be created at a radio frequency (at which the technical noise of the laser is vanishing) and subsequently detected by a lock-in amplifier. This signal will be digitized into pixel intensity, and collectively an image will be obtained by raster scanning of the laser beams across the sample. Because detection sensitivity, imaging speed, and spatial resolution are three key considerations in evaluating microscopy, next we discuss them to provide a basic evaluation of this emerging microscopy.

Detection sensitivity

Firstly, as the initial motivation to use stimulated emission, the sensitivity of SRS is multiple orders of magnitude better than the spontaneous Raman. Besides, thanks

to the high-frequency modulation, SRS detection is immune to noise, such as laser fluctuation and fluorescence background, at low frequency. Typically, the detection limits of SRS microscopy are around μM to mM.[52] The exact sensitivity closely depends on the Raman spectrum, such as the cross-section of individual chemical bonds (σ_{Raman}) and the number of bonds (N_s) presented. Because Raman scattering originates from the polarizability change during oscillation, non-polar bonds generally show stronger Raman cross-sections than polar bonds. Hence, the backbone bonds, such as C=C, C≡C, C≡N, and C=O, become hot spots for imaging.[53–55] Other bonds, such as C-H, due to its high abundance in organic compounds, are also highly favored for imaging.[56] C-H bond energy is easily affected by other surrounding atoms and thus suitable to be imaged to reveal the reaction process. Meanwhile, various bonds in inorganic materials have also been reported with high sensitivity, such as P-O,[43] B-N,[21] S-H,[32] and B-H.[57] For example, the stretching vibration of B-H has been used to image the distributions of boron-based drugs in HeLa cells to study its uptake conditions.[57]

Imaging speed

Although conventional spontaneous Raman can be coupled to a microscope, the imaging/mapping speed is severely restricted by its low sensitivity. It usually takes seconds to reach an adequate signal-to-noise ratio at a single pixel, and consequently hours to complete an image. This time-consuming process further makes the imaging quality suffer from the physical motions of samples. More importantly, slow acquisition speed deprives the system of the capability of capturing fast dynamics. Spontaneous Raman microscopy can only track slow material dynamics on the scale of minutes to hours, but chemical reactions and transport in material systems are often in the timescale of seconds or shorter. With the dramatically enhanced sensitivity, SRS microscopy can reduce the dwelling time at a pixel to merely several microseconds. A frame with 512 × 512 pixel resolution only takes a few seconds, and even video-rate (>30 Hz) imaging can be achieved,[30,58] enabling the study of fast dynamics inside materials.

Spatial resolution

SRS microscopy can use a commercial confocal microscope as the scanning system. This implies: (1) that its spatial resolution resembles that of two-photon fluorescence microscopy, as the stimulated scattering events can only happen around the focus where the density of photons is maximized[59]; and (2) that SRS imaging is intrinsically capable of 3D optical sectioning. The SRS signal collected by the detector is purely from the focal plane. Regarding the diffraction-limited resolution, a typical SRS microscope uses NIR lasers for excitation (wavelength ~800–1,064 nm). The resulting lateral spatial resolution is around 300 nm and the axial resolution is ~1 μm under objectives with a high numerical aperture.[32] However, spatial resolution can be enhanced by reducing laser wavelength to visible light (e.g., frequency doubling of 1,064–532 nm), as discussed in the next section.

Recent advances in the instrumentation of SRS microscopy

The unique physical principles and instrumentation render SRS microscopy an advanced imaging tool for scientific studies. Since its invention, extensive efforts have been made to optimize the performance of SRS microscopy to fit into broad imaging applications. These parameters include, but are not limited to, detection sensitivity, imaging speed, spatial resolution, and volumetric imaging. Here we focus the discussion on recent technical advances and the fast-evolving performance of SRS microscopy.
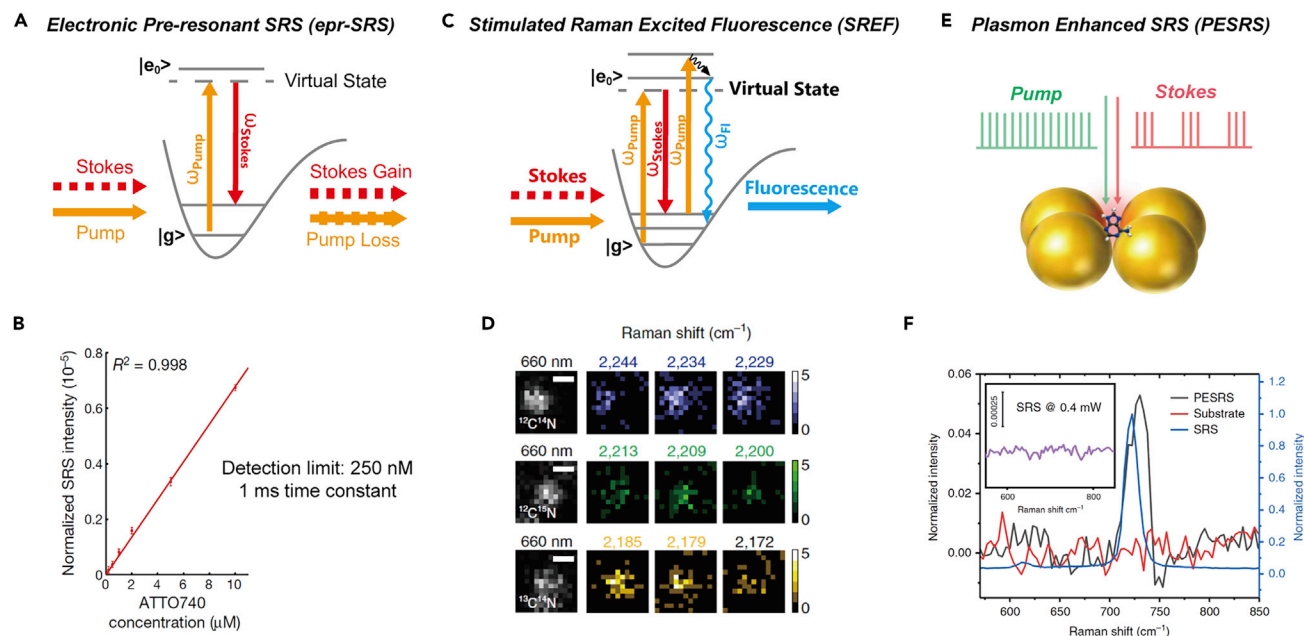
Figure 3. Recent advances to boost the sensitivity of SRS

(A) The principle of electronic pre-resonant SRS (epr-SRS). g and e_0 represent the ground and excited electronic states, respectively.

(B) Plot shows the linear dependence of the epr-SRS signal on the concentration of Atto-740, a near-infrared chromophore. The detection limit was determined to be 250 μM.[23]

(C) The principle of stimulated Raman excited fluorescence (SREF).

(D) Single-molecule imaging of three Rh800 isotopologs. Scale bars, 400 nm.[60]

(E) Plasmon-enhanced SRS (PESRS) greatly enhances the cross-sections of molecules conjugated on the substrate surface.

(F) Background-subtracted PESRS spectrum of adsorbed adenine (total power, 0.4 mW) versus the SRS spectrum of adenine powder (pump power, 10 mW; Stokes power, 50 mW) and the spectrum of the blank substrate. Inset: the SRS spectrum of adenine powder obtained at the same laser power condition as the PESRS.[61]

Improvement in chemical sensitivity

As a far-field imaging method, SRS is compatible with the aforementioned near-field enhancements. The coalition of stimulated scattering with either resonant enhancement or surface plasmon can further boost the sensitivity of a microscope. In 2017, electronic pre-resonance SRS was first demonstrated by the Min group (Figure 3A).[23] When the pump wavelength gets close to but does not hit the electronic resonance of molecules, which are typically visible chromophores, the Raman cross-section can be dramatically amplified. The experimental results (Figure 3B) suggested a sub-micro-molar detection limit, equal to 100 molecules in the focal volume (~0.1 mm^3). Based on similar concepts, stimulated Raman excited fluorescence (SREF) microscopy was invented 2 years later (Figure 3C).[60] By up-converting the vibrational excited states to electronic excited states, the excited molecules will end up in a state of relaxation to any vibrational states of ground electronic states, leading to emission of fluorescence. The vibrational signal can be transformed into fluorescence emission events so that the sensitivity can be further improved. The authors achieved single-molecule imaging of Rh800, a nitrile-bearing NIR dye. By leveraging the superb sensitivity of SREF, they achieved the first all-far-field single-molecule Raman spectroscopy and imaging without plasmonic enhancement (Figure 3D). On the other hand, the Cheng group published their work on boosting SRS signals through plasmon enhancement, and the technique was named plasmon-enhanced SRS (PESRS) microscopy in 2019.[61] By anchoring adenine on the surface of gold nanoparticles and implementing background subtraction and denoising algorithms, single-molecule detection was successfully achieved (Figures 3E and 3F). Such an ultrasensitive detection method

coupled with the SRS microscopy has granted a bright future for mapping and tracking fast chemical dynamics at the molecular level.

Broader spectrum and higher scanning speed

Conventional SRS microscopy with a picosecond OPO laser source can only detect one wavenumber at a time. It requires several seconds to achieve broad wavelength tuning, as the temperature control of the nonlinear crystal inside OPO limits the overall tuning speed.[62] Thus, wavelength sweeping may take a long time to achieve the final hyperspectral imaging. This is undesirable for extensive topics in materials science since spectral information is critical to understanding variations in chemical bonds. To accelerate imaging across multiple vibrational modes, several methods were proposed and proved. For example, a broadband femtosecond laser with pulse shaping can be used to rapidly select desired frequencies with spectral filters (Figure 4A).[30] A video-rate imaging covering a wide spectral window of 300 cm^{-1} was demonstrated with a spectral resolution down to 4 cm^{-1}. The spectral images can be interpreted using independent component analysis, thus providing both spectroscopic details and spatial distributions (Figures 4B and 4C). Another powerful method is spectral-focusing by linearly chirping two broadband femtosecond lasers and decoding the spectral information from time delay.[56,63] As reported, an SRS spectrum of 200 cm^{-1} can be acquired in 83 μs. Beyond tuning the excitation lasers, multi-channel array detectors and lock-in demodulation can be utilized to achieve multi-mode detection, thus speeding up the imaging process.[64,65]
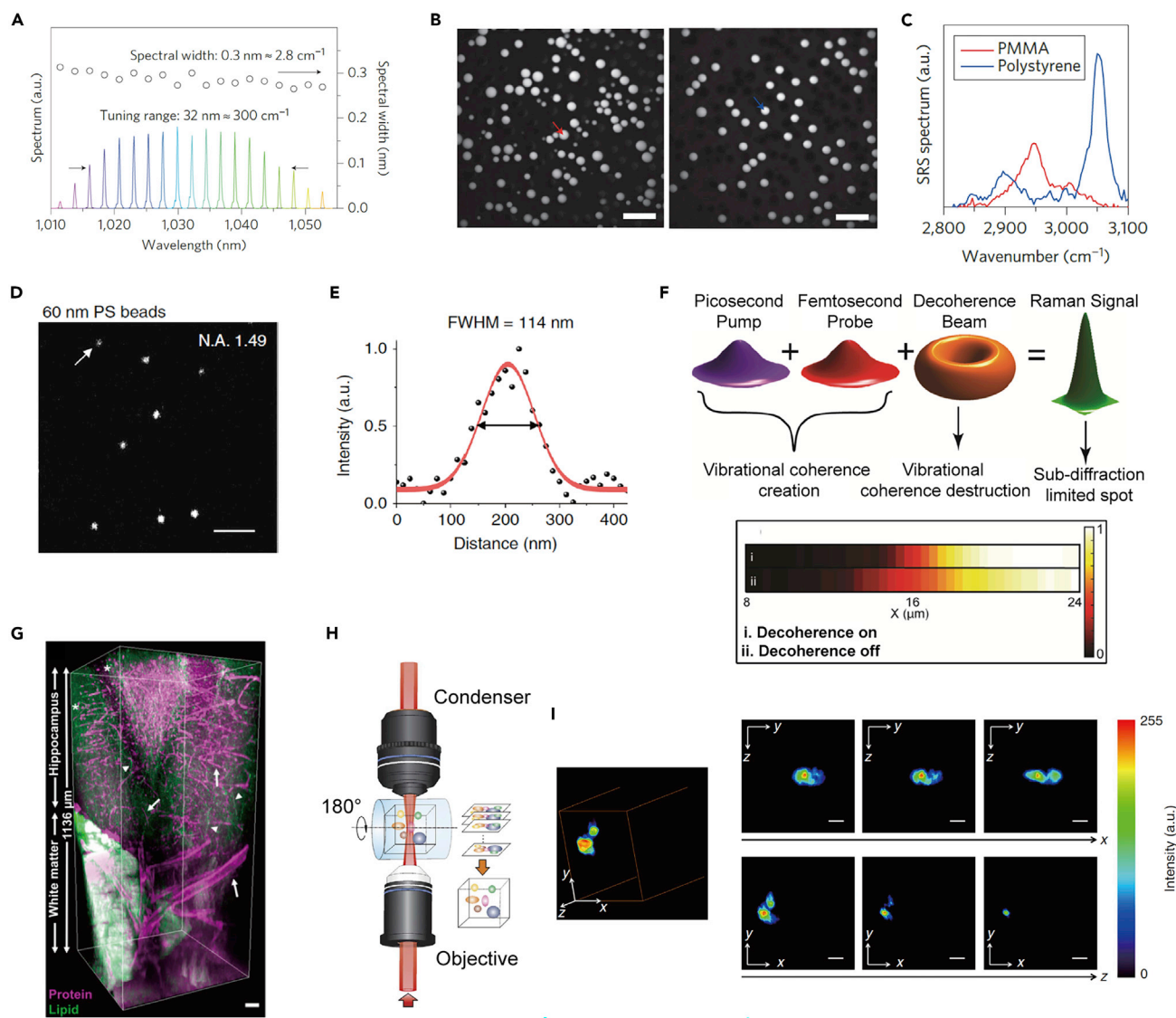
Enhancing spatial resolution

The spatial resolution of Raman microscopy, which is diffraction limited, depends on the wavelength of light. Therefore, using lasers of shorter wavelength should further improve the resolution. This idea was demonstrated in 2018 by the Wang group.[66] By doubling the frequencies of both lasers, a lateral resolution of 130 nm was achieved (Figures 4D and 4E). Meanwhile, breaking the diffraction limits has long been appealing for every optical technique. Learning from the well-known super-resolution method, stimulated emission depletion fluorescence, several models of super-resolution SRS were proposed. By applying an extra donut-shaped beam to suppress the peripheral SRS signal through depletion, a sub-diffraction-limited lateral resolution was achieved on a diamond plate sample (Figure 4F).[67]

3D reconstruction

Through the axial direction, NIR light generally bears better penetration capability. Together with optical sectioning, SRS is capable of volumetric 3D imaging with great imaging depth. In biomedical practices, SRS microscopy can be combined with clearance techniques to achieve superb imaging depth, and its applications in animal tissue imaging have been well demonstrated (Figure 4G).[68] It allows a thorough investigation of fine structures inside a sample. In 2017, the Cheng group[69] reported their progress in volumetric SRS imaging with a Bessel beam. Stimulated Raman projection microscopy can achieve fast 3D imaging through a two-dimensional lateral scan (Figures 4H and 4I). Combining such a scan method with sample rotation, 3D tomography of chemical compositions can be readily reconstructed.

APPLICATIONS OF SRS MICROSCOPY IN MATERIALS SCIENCE

The high chemical sensitivity, high imaging speed, and fine spatial resolution of SRS microscopy make it valuable instrumentation for material studies. As well as the key merits mentioned above, several other noteworthy properties render SRS microscopy attractive for materials science. The first is label-free imaging. SRS does not require any specialized labels or probes commonly needed for other optical imaging methods,

Figure 4. Advances in SRS on improving imaging speed, spatial resolution, and volumetric imaging

(A) Using a picosecond pump laser and a broadband femtosecond Stokes laser as excitation sources. The spectral filter can rapidly generate desired narrowband output thus reaching fast spectral tuning and wide spectral scanning range of 300 cm^{-1}.[30]

(B) The hyperspectral imaging of polystyrene (PS) and Poly(methyl methacrylate) (PMMA) microbeads at the spectral window generated in (A). Scale bars, 20 μm.

(C) Spectra of PMMA and PS taken at locations indicated by the red and blue arrows in the images.

(D) SRS imaging of C-H stretching mode using frequency-doubled pump and Stokes beams.Scale bar, 1 μm.

(E) Cross-section profile of a selected PS bead indicated by the arrow in (D). [66]

(F) Using a donut-shaped beam profile to achieve super-resolution SRS imaging. The image shows a Raman signal across a diamond plate edge. The addition of a donut-shaped decoherence beam improves the spatial resolution.[67]

(G) Three-dimensional reconstruction of the hippocampus and white matter. Arrows indicate vasculatures, arrowheads indicate axons, and stars indicate cell bodies. Scale bar, 50 μm.[68]

(H) Stimulated Raman projection (SRP) tomographic imaging with a Bessel beam. The sample can be rotated along the lateral axis to achieve a fast volumetric scan and 3D reconstruction.

(I) SRP imaging of a single 3T3-L1 cell. The image on the left shows a 3D-reconstructed 3T3-L1 cell. Other images are selected 2D views from sagittal or transverse directions. Scale bars, 20 μm.[69]

such as fluorescence microscopy. The vibrational mode itself serves well as a fingerprint of chemical bonds. Secondly, as an optical imaging technique, SRS microscopy is non-intrusive to samples, enabling *in situ* studies on the dynamics of material systems. For

instance, it is capable of *operando* monitoring of an electrochemical cell.[22] Thanks to these merits, SRS microscopy has generated fruitful results in various material topics, such as batteries, 2D materials, zeolites, aerosols, catalysts, and polymers. These studies demonstrate the potential of SRS, provide fundamental insights into materials science, and help design better materials and devices. In this section, we review recent progress on using SRS microscopy for various material topics. Based on whether temporal evolution and chemical transformation are involved or not, we categorize the past studies into three regimes from static samples to dynamic phenomena: (1) static material structures, (2) transport of chemical species, and (3) transformation in chemical reactions.

Static material structures

Compared with spontaneous Raman microscopy, the major advantage of SRS microscopy for imaging static materials is its high scanning speed. The acquisition time for a single pixel with a spontaneous Raman microscope is typically 0.1–1 s, three orders of magnitude longer than an SRS microscope. Hence, it only takes seconds for an SRS microscope to acquire an image, but minutes and even hours for spontaneous Raman microscopy to do the same job. Although SRS microscopy can only image one, two, or a narrow range ($\sim$200 cm^{-1}) of wavenumbers at a time, two to ten wavenumbers are often enough for understanding material structures. Therefore, SRS microscopy is highly attractive for high-throughput and large-area structural analysis. So far SRS microscopy has been used to study many materials, as discussed below. These results demonstrate the high chemical, temporal, and spatial resolution of SRS in 3D profiling.
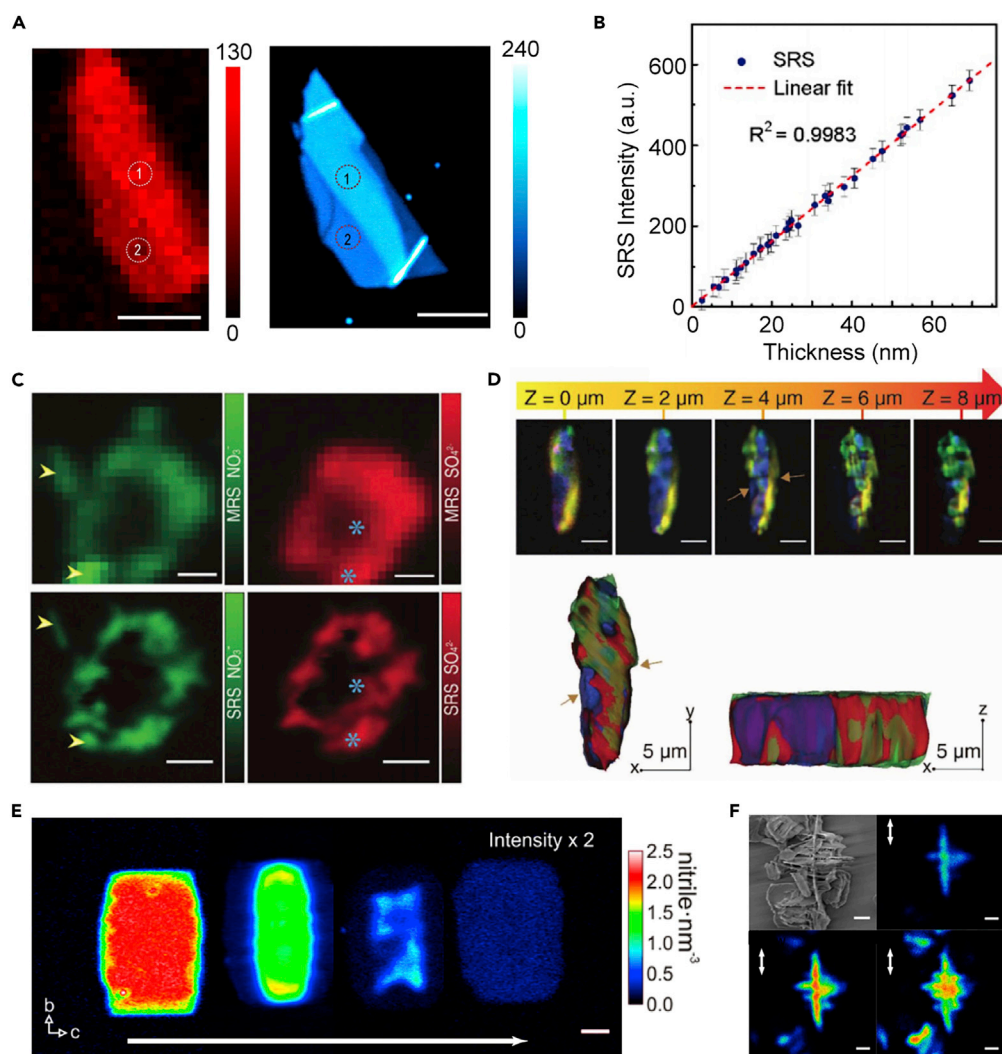
2D materials

2D materials, such as h-BN nanosheets, usually suffer from low Raman scattering due to their small thicknesses. SRS can quickly obtain critical information of 2D materials, such as thickness, dopants, defects, and strains, which enables high-throughput characterizations. The Ji group[21] used an SRS microscope for large-scale chemical mapping of h-BN with the E_{2g} vibration mode at 1,367 cm^{-1}. While it takes 40 min to acquire a 20 × 30 pixel image using a spontaneous Raman microscope, only 30 s is needed to acquire a 320 × 320 pixel image using an SRS microscope, which is 13,000 times faster (Figure 5A). By imaging BN nanoflakes with different thicknesses, they found that the SRS signal intensity is independent of polarization and highly proportional to the number of layers of h-BN; thus, the thickness distribution of h-BN flakes can be quickly determined using SRS images (Figure 5B).[21]

The same group also used SRS to characterize the uptake of MoS$_2$ nanosheets in living cells.[70] MoS$_2$ nanosheets were reported to have an optical transient absorption (TA) in the NIR range; therefore, a dual-mode microscope with both TA and SRS was developed to simultaneously image the organic component and uptake condition of inorganic MoS$_2$ nanosheets in the cell. They found that smaller MoS$_2$ nanosheets can more easily enter a cell. The MoS$_2$ nanosheets taken up concentrate in the cytoplasm and mainly exist as small aggregates, while loaded drugs can be found in the whole cell, including the nucleus. This may suggest that drugs may enter the cell nucleus after being released from their nanocarriers. Eventually, MoS$_2$ nanosheets colocalize with intracellular lipids. This work shows the process and fate of MoS$_2$ nanosheets as drug carriers. MoS$_2$ nanosheets may become a useful label for material studies by SRS microscopy in the future.

Aerosols

Visualizing the 3D chemical profiles of aerosols is crucial to understanding their formation mechanisms and aging processes. Ao et al.[18] applied SRS microscopy to

Figure 5. Imaging static material structures

Imaging static material structures of (A and B) 2D h-BN nanoflakes,[21] (C and D) aerosols,[18] and (E and F) zeolites by SRS microscopy.[20,41]

(A) The comparison of the same h-BN nano-flake under a spontaneous Raman microscope (red) and an SRS microscope (blue). Scale bars, 10 μm. The numbers on the color bars indicate Raman intensity or SRS intensity.

(B) The SRS intensity is strictly linear with the thickness of h-BN nanoflakes.

(C) The comparison of aerosols under a spontaneous Raman microscope (upper) and an SRS microscope (lower). For the spontaneous Raman imaging, it takes 2.5 h for a 30 × 30 pixel image, while it only takes 2 s under a two-color SRS microscope. Scale bars, 2 μm.

(D) The SRS imaging and 3D reconstruction of individual synthetic particles in aerosols, showing the spatial distribution of nitrate (green, 1,065 cm^{-1}) and sulfate (red, 982 cm^{-1}).Scale bars, 5 μm.

(E) Chemical mapping of PhCN adsorbed in hydrogen-exchanged mordenites revealing the accessibility of acid sites inside. From left to right: small-port mordenite (SP-MOR), early stage, intermediate stage, and strongly dealuminated mordenite (SD-MOR). The wavenumber of the fingerprint C≡N stretching bond here is 2,275 cm^{-1}. Scale bars, 3 μm.

(F) An SEM image of hierarchical silicalite-1 crystals (top left) and corresponding SRS images at different depths of organic structure-directing agent molecules inside micropores of the crystal. Scale bars, 1 μm.[41]

image the 3D chemical profile of aerosols in a non-intrusive manner. Compared with the conventional spontaneous Raman microscopy, SRS microscopy can achieve an imaging speed 4,500 times faster so that finer structures of aerosols can be determined in a short time (Figure 5C). Meanwhile, the 3D optical sectioning and multi-channel capability of SRS microscopy allow 3D reconstruction of compositional and structural information in aerosols (Figure 5D). Thanks to the high speed of

SRS, high-throughput quantifications of particle sizes in aerosols were realized by large-area imaging and statistical analysis. The authors showed that the quantification of nitrate and sulfate salts using an SRS microscope was comparable with traditional ion chromatography (IC), and exhibited advantages over IC in terms of speed, non-intrusiveness, and size-distribution analysis. Furthermore, 3D profiling of aerosol particles showed that nitrates tended to partially coat on sulfates. This study shows the advantage of SRS on scanning speed and 3D imaging capability, demonstrating its potential in high-throughput analysis for material studies.

Zeolites

Zeolites are important materials as they have wide applications in catalysis and chemical separation.[71] The accurate structure of zeolites is fundamentally important since it is critical to diffusion pathways of gases and adsorption/desorption kinetics, which ultimately determine their performance. SRS microscopy is a powerful tool to study these processes given its high spatial/chemical resolution and 3D sectioning capability. For example, hydrogen-exchanged mordenites are usually de-aluminized to increase their mesoporosity and their performance as catalysts in petrochemical industries, but how dealumination affects the properties of zeolite is unclear. Liu et al.[20] used SRS microscopy to study the acid distribution and accessibility in zeolites at different dealumination stages. In their studies, D-acetonitrile (CD$_3$CN) and benzonitrile (PhCN) were used as the probes because they contain C≡N stretching bonds that can access all the acid sites inside zeolite. They found that adsorbed nitrile was symmetrically oriented in the side pockets and isotropically distributed in the main channels. The acid sites decreased with increasing dealumination, and are easier to remove in the main channel than in the side pockets. The surface was preferentially dealuminated due to more main channels near the surface. Therefore, the acid sites were heterogeneous at the early stage and the intermediate stage during dealumination, and these sites eventually turned homogeneous at full dealumination (Figure 5E). This work unraveled the complex framework of aluminum removal in zeolite using SRS and can be applied to other studies, such as the physicochemical properties of heterogeneous catalysts. Along this line, Fleury et al.[41] studied how a diquaternary ammonium cation agent helped form a hierarchical silicalite zeolite using SRS microscopy. Once bonded with two quaternary ammoniums, the vibrational mode of CH$_2$ shifts from 2,915 to 2,884 cm^{-1}; and thus it can be imaged to reveal the location of the diquaternary agent inside the framework (Figure 5F). They found that the structure-directing diquaternary ammonium cation agent preferentially locates in linear pores rather than zigzag pores of the zeolite. These results can guide the design of new hierarchical zeolites.

Minerals and environment

SRS microscopy is also attractive for studying mineral and environmental materials since it can enable fast, high-throughput, and 3D profiling of these materials (e.g., plastics, salts), which remarkably reduces the time needed for sample statistics and accelerates research in relevant fields. For example, Houle et al.[19] studied quartz and calcite using an SRS microscope. They revealed trapped organic inclusion in quartz minerals by imaging the fingerprint C-H bond with an SRS microscope. Using SRS, the composition of a quartz/calcite mixed sample can be quickly determined (Figure 6A). Zada et al.[27] used SRS to study plastic microparticles in the environment, such as nylon, polyethylene terephthalate, polyethylene, and polypropylene. By imaging the signature peak of each type of plastic (Figure 6B), SRS could quickly determine the chemical nature of plastic microparticles at a speed 1,000 times faster than a conventional spontaneous Raman microscope. Similarly, Laptenok et al.[72] used an SRS microscope for fast and reliable classification of microfibers
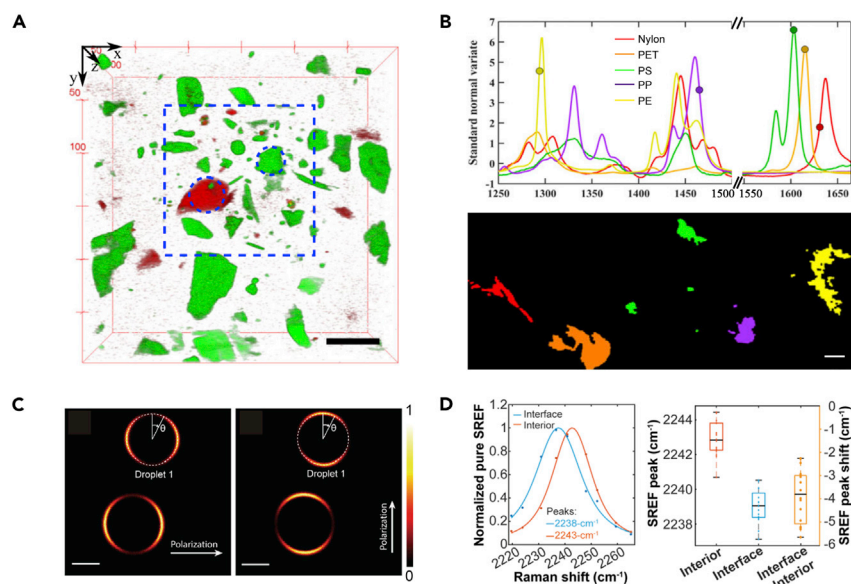
Figure 6. SRS imaging of environmental samples, minerals, and the water/oil interface

(A) A 3D SRS image of calcite (1,088 cm^{-1}, green) and quartz (466 cm^{-1}, red) powders fixed in cyanoacrylate.[19] The region of interest probed is 300 × 300 × 100 μm. Scale bar, 50 μm.

(B) Top: Raman spectra of five target polymers. The circles indicate the wavenumbers (1,631, 1,615, 1,603, 1,465, and 1,294 cm^{-1}) selected for the SRS image at the bottom. PET, polyethylene terephthalate; PS, polystyrene; PP, polypropylene; PE, polyethylene. Bottom: five identification images of these polymers were colored and overlaid. Red, nylon; orange, PET; green, PS; magenta, PP; and yellow, PE. Scale bars, 100 μm.[27]

(C) Two-photon fluorescence images of microdroplets containing 2 μM Rh800 in hexadecane with different perpendicular excitation laser polarization (left, horizontal direction; right, perpendicular direction). Scale bars, 5 μm.

(D) Left: background-subtracted SREF spectra of the C≡N stretching mode in the interior of a water microdroplet (red curve, 2,243 cm^{-1}) and at the oil/water interface (blue curve, 2,238 cm^{-1}). Right: boxplot of 16 independent measurements of the Rh800 nitrile peak positions in the interior of water microdroplets and at the oil/water interface. The right y axis labels the corresponding Stark shifts.[24]

from different environmental samples, such as paper, linen, cotton, and polymers. The signature peaks of these fibers are determined first, then the environmental fibers from drinking water, surface water, and sea sediment can be quickly identified by using an SRS microscope to image their corresponding peaks. SRS microscopy evaluates pollution sources in a real-time detection manner, and thus provides timely advice for pollution control.

Liquid/liquid interfaces

Water microdroplets have been long known to exhibit distinct kinetic and thermodynamic properties from those of bulk water, and it was postulated that a strong local electric field associated with the curvature of droplets accounted for such unusual features.[73,74] However, due to limitations in instrumentation, the electric field cannot be directly probed and determined on water microdroplets. In 2020, Xiong et al.[24] utilized SREF microscopy to measure the electric field-driven Raman shift (i.e., Stark effect) of the Rh800 probe at the interface between water and oil. The imaging results showed that Rh800 dyes concentrated at the interface of a water droplet immersed in the oil matrix (Figure 6C). The hyperspectral SREF imaging revealed a 4 ± 1 cm^{-1} redshift of the C≡N stretching mode in Rh800 at the interface compared with the bulk water phase (Figure 6D), indicating the existence of a strong

electric field across the interface. The further quantitative analysis determined the field to be as strong as $\sim 10^7$ V/cm. The shift resulted from a very local effect, which can be attributed to both electric fields formed by a charged ion double layer, and some more intimate interactions, such as a hydrogen bonding effect. Nonetheless, they are all static electric interactions, which in sum formed the local electric fields sensed by the probe molecule. This direct observation of the electric field provided a compelling mechanism to account for the unusual kinetics of chemical reactions on the microdroplet surface.

Transport of chemical species

Transport of chemical species is critical to many material processes and phenomena, such as energy storage and conversion, gas separation, microfluidics, and material manufacturing. Such chemical transport can be driven by various factors, including concentration gradients, external fields (e.g., thermal, electrical), and perturbations (e.g., convection). Taking concentration-driven diffusion as an example, the diffusivity of chemical species can be as high as 10^{-8}–10^{-4} cm^2/s (e.g., 10^{-6} cm^2/s for Li$^+$ in liquid organic electrolytes,[75] and 10^{-8} cm^2/s for gas diffusion in the metal-organic framework [MOF][76]), so it only takes ~ 1 ms to diffuse 1 μm. Moreover, the concentration of target species may be very low. For example, during the ion depletion in a battery electrolyte, the ion concentration near the electrode surface can be as low as 1–10 mM.[22,75] Such a low concentration is below the detection limit of a wide range of microscopies in materials sciences, such as electron microscopes, MRI, and synchrotron imaging tools. Besides, it is ideal that the microscopy technique can be operated *in situ* or *in operando* as chemical transport is often a transient process.

SRS microscopy is attractive to fill the gap on temporal resolution and spatial resolution for characterizing the transport of chemical species, particularly those with low chemical concentration. One recent study on this topic was to use SRS microscopy to image ion depletion in a battery electrolyte and its correlation with the growth of lithium dendrites. As discussed above, such a process requires an acquisition time of 1–10 s, a low ion concentration of <100 mM, and a fine spatial resolution of 1 μm or less. Hence, it is difficult to be characterized by conventional imaging tools, including spontaneous Raman microscopy. In contrast, the merits of SRS microscopy make it a suitable tool to address these challenges and provide a better understanding of ion depletion and electrode/electrolyte interactions at the interface.

To realize such *operando* imaging, Cheng et al.[22] sandwiched a Li/gel electrolyte/Li planar cell between two glass slides, sealed it by using epoxy, and placed it under an SRS microscope (Figure 7A). Lithium bis(oxalato)borate (LiBOB) was chosen as the salt because C=O has a strong vibrational mode (1,830 cm^{-1}) in the optimal detection region. Therefore, the signal-to-noise ratio (SNR) is high, and the SRS signal is linearly proportional to the concentration of BOB$^-$ ([BOB$^-$]). [Li$^+$] is considered to be equal to [BOB$^-$] due to the requirement of electro-neutrality, even at the depletion stage (Figure 7B).

The authors successfully visualized ion depletion in a battery electrolyte and how it interacts with lithium dendrite growth for the first time, an important topic in battery studies (Figure 7C).[22] The work unveiled a three-stage growth mechanism of lithium deposition: no depletion; partial depletion; and full depletion (Figure 7D). A positive feedback mechanism between dendrite growth and local concentration of Li$^+$ ions was also illustrated, which cannot be seen without imaging the ion profile by SRS. Inspired by these findings, a Li$_3$PO$_4$ solid electrolyte coating on the Li surface was
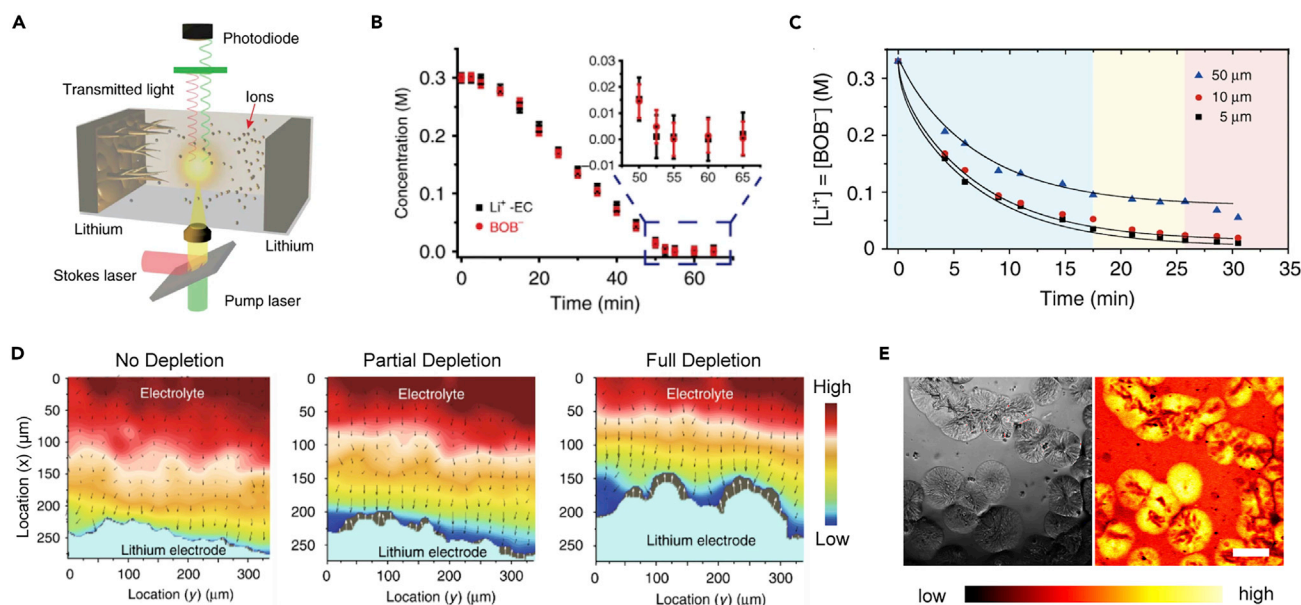
Figure 7. Using SRS microscopy to study the ion depletion and lithium dendrite growth *in operando*

(A) A schematic illustration of a Li–Li symmetric cell under SRS imaging.

(B) The changes of Li$^+$ and BOB$^-$ concentrations during ion depletion near a lithium electrode. The concentrations are interpreted from spontaneous Raman spectra.

(C) The Li$^+$ concentration near lithium metal surface versus time.

(D) The ion concentration and dendrite growth acquired using an SRS microscope at three representative stages: no depletion, partial depletion, and full depletion.

(E) The bright field and corresponding SRS images of a lithium metal/PEO polymer electrolyte interface during lithium plating. Scale bars, 50 μm.[22]

applied to homogenize ion distribution and led to a more uniform deposition of lithium regardless of the depletion of Li$^+$ ions. Such observation of dynamic ion transport in battery electrolytes can be further extended to other liquid/gel electrolytes, polymer electrolytes (Figure 7E), and polymer/ceramic composite electrolytes for various systems (e.g., Li-ion, Na-ion, Zn-ion, alkaline batteries, fuel cells, and electrolyzers).

Currently, SRS microscopy has not been widely explored for tracking chemical transport, but various other transport processes have been studied by related microscopies, such as transport of chemical species in MOF by IR microscopy[77] and fluorescence microscopy.[78] We believe that these systems can also be studied by SRS, which could provide valuable information (e.g., high spatial, temporal, and chemical resolution) to better understand these systems.

### Transformation in chemical reactions

Chemical reactions are often accompanied by changes in bonding and/or local chemical environment. Such changes will affect vibrational modes, leading to the creation, disappearance, or shifts of Raman peaks. SRS microscopy can monitor the intensity variations of Raman peaks and provide fine information on the fast dynamics of such chemical transformation. In the literature, several chemical reactions have been explored by imaging signature Raman peaks, as detailed below, and we believe that SRS can be extended to study a broad range of reactions in the future.

Polymerization is an important but complicated process. Its formation mechanism is difficult to resolve, particularly regarding how polymerization initiates and

propagates. To better understand this process, Li et al.[25] developed a collinear multiple-beams SRS microscope with a high scanning rate of 2,000 frames per second to visualize the fast dynamics of polymerization. The polymerization of acrylamide triggered by the crosslinking agent N,N'-methylenebisacrylamide was investigated (Figure 8A). First, the spontaneous Raman spectrum showed that the H-C-H peak shifts from 3,043 cm^{-1} in acrylamide to 2,928 cm^{-1} in polyacrylamide, and so this peak was chosen as a label to image the polymerization process (Figure 8B). The authors observed that polymerization initiated and spread quickly under continuous UV exposure within 4 s (Figure 8C). After 18 s, spiny structures started to appear and branches formed, whose growth speed was proportional to the power of the UV laser. The authors further increased the imaging speed to the millisecond level to better understand the initial polymerization of acrylamide. Feather-like structures appeared, with rich stochastic branches, at the beginning of polymerization, showing that the radical chain was prone to remain growing along a specific direction until the termination of polymerization. Such observations deepen our fundamental understanding of the polymerization process and could provide new insights into how to control the morphology of final products.

SRS imaging has also been used to image chemical transformation in pharmaceutical materials, such as their degradation and polymorphs. The fast speed of SRS imaging provides a convenient approach to quickly and quantitatively detect the level of drug degradation during storage. Figueroa et al.[45] used SRS to study the disproportionation reaction of pioglitazone hydrochloride (PIO-HCl), a diabetes type II treatment, to PIO free base (PIO-FB) under moisture. PIO-HCl and PIO-FB have different signature peaks at 1,610 and 1,640 cm^{-1}, respectively, due to the protonation, making them distinguishable in SRS imaging (Figure 8D). The authors found that the disproportion was solution mediated through water, and the disproportionation preferentially happened on the surface rather than in the bulk under moisture. In addition, physical contact was not required between magnesium stearic and PIO-HCl for the disproportionation process to happen. This was one of the first examples of using SRS microscopy to investigate the molecular interplay between drug substances and excipients in pharmaceutical tablets.[45] Sarri et al.[26] used SRS to examine polymorphs of medicines, including clopidogrel, a heart medicine, and amibegron, an antidepressant. Polymorphs of clopidogrel and amibegron can be distinguished using wavenumbers of 3,098 cm^{-1}/3,109 cm^{-1} and 3,055 cm^{-1}/2,974 cm^{-1}, respectively. With these different signature peaks, two polymorphs of the active ingredient along with excipients in the medicine can be simultaneously mapped (Figure 8E). The authors show that SRS imaging can quickly characterize pharmaceutical tablets to determine the ratio of effective polymorphs, and examine their stability over time (Figure 8F). Haasterecht et al.[79] also successfully imaged silicone debris in tissues using an SRS microscope. They found that large silicone particles existed in sizable tissue vacuoles and silicone debris might migrate to distant organs (Figure 8G). They discussed the possible formation mechanism of the silicone debris, which helps to investigate the role of silicone debris in implant-linked diseases.[79]

SRS imaging also has a great potential to study chemical transformation in catalysis, such as the generation of intermediate products and the dynamic diffusion of reactants and products in solution. While there is still no report on this direction, SRS spectroscopy has been used by Eom et al.[43] to study the formation and structure of oxygen evolution reaction catalyst. In this work, amorphous cobalt oxide deposited in a phosphate electrolyte (CoPi) was studied with ^{18}O isotope as the label. The authors found that the orthophosphate species (PO_4^{3-}) formed a network like a glass, which surrounded the cobalt oxide nanoclusters and functioned as the active
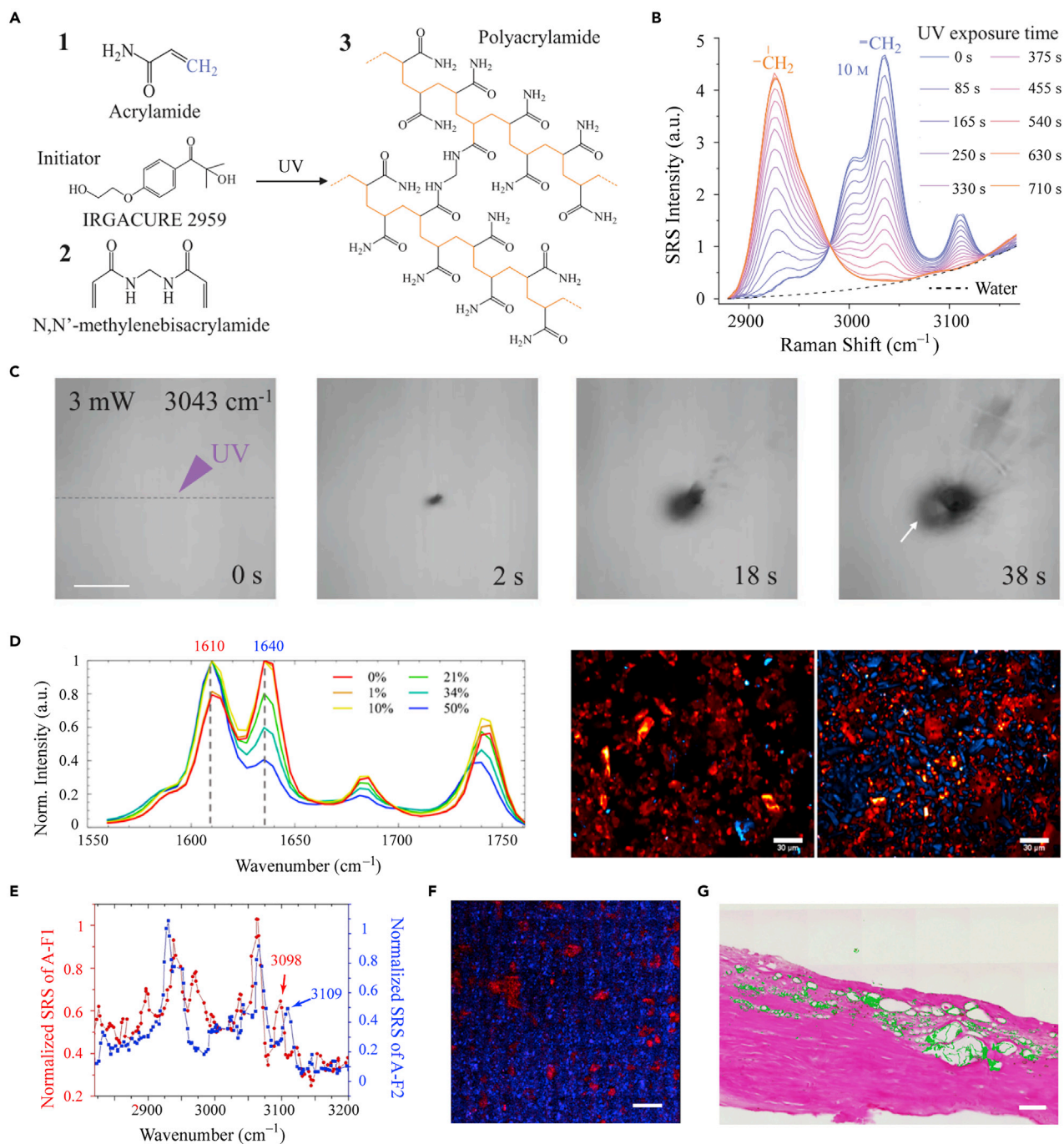
Figure 8. Progress on using SRS microscopy to study polymerization processes and pharmaceutical tablets

(A) Schematics of UV laser-induced hydrogel polymerization.[25]

(B) The temporal evolution of the Raman spectra of acrylamide and polyacrylamide during polymerization.

(C) SRS images of the fast polymerization of polyacrylamide. Arrows indicate the polymer wave. Scale bars, 25 μm.

(D) Measured SRS spectra and SRS images of a mixture of PIO-HCl and PIO-FB. PIO-HCl and PIO-FB are represented in red (1,610 cm^{-1}) and blue (1,640 cm^{-1}), respectively. Scale bars, 30 μm.[45]

(E) SRS spectra of two clopidogrel polymorphs. 3,098 cm^{-1} (red) and 3,109 cm^{-1} (blue) are the fingerprint peaks for differentiating the two polymorphs in SRS imaging.

(F) The corresponding SRS image of the two clopidogrel polymorphs in (E). Scale bar, 100 μm.[26]

(G) SRS of breast tissues containing silicone. Scale bar, 100 μm.[79]

🗝 CellPress

reaction sites in CoPi. They further speculated that this unique structure was formed via the electrogeneration of high-valence Co ions.[43] In the future, the combination of SRS imaging with spectroscopy studies could further unveil the spatial heterogeneity of catalysts and deconvolute reaction mechanisms in heterogeneous catalysis.

PERSPECTIVES

SRS microscopy has shown exciting capabilities for better characterizing and understanding a broad range of topics in materials science, as demonstrated by the emerging examples discussed above. As SRS microscopy was originally targeted for biomedical applications, most existing SRS microscopes are not optimized for materials research. Hence, we believe that there are great opportunities ahead in not only enhancing the instrument's capability for material studies, but also unveiling unprecedented information in material structures, properties, and processes. In this section, we discuss our perspectives on future directions in applying SRS microscopy to materials science. Based on the nature of these directions, we divide them into three categories: (1) optimization of SRS microscopes for materials science, (2) advancement of instrumentation for enhancing the detection limit and resolution, and (3) future research topics in materials science.

1) Optimization of SRS microscopes for materials science.

First, the wavelength and power of the light source need to be considered. Current SRS microscopes typically use NIR light sources to better penetrate cells and tissues for biological studies; however, SRS microscopes can use visible light to enhance spatial resolutions for material studies. Bi et al.[66] have demonstrated an SRS microscope with 450 and 520 nm lasers serving as pump and Stokes lasers, respectively, and a spatial resolution of 130 nm is achieved. Such improvement in spatial resolution is important for materials science. Regarding the beam power, the high power used in current SRS builds may potentially cause photodamage and thermal effects to the sample, which has not yet been clearly studied. The quantification of such effects will greatly help appropriate power selection, particularly when the sample is delicate or sensitive to local temperatures.

Second, the range of wavenumbers must be considered. Most SRS microscopes are optimized in the wavenumber range between 1,200 and 3,600 cm^{-1}, since this range includes most signature peaks in biological samples (e.g., C-H, C=O, C=C, S=O, O-P-O).[32] Moreover, this range includes the so-called cell-silent regime (1,800–2,800 cm^{-1}), which can be used for detecting isotope-labeled bonds and triple bonds (e.g., C-D at ~2,100 cm^{-1} and C≡N at ~2,250 cm^{-1}).[32] Meanwhile, most significant peaks in inorganic materials are below 1,000 cm^{-1} (e.g., P-F stretching of PF_6^- anions [770 cm^{-1}],[80] Li^+-propylene carbonate interaction [741 cm^{-1}],[81] and Zn-O stretching in zincate [471.2 cm^{-1}][82]) due to the involvement of heavier atoms. Therefore, the optical circuit should be redesigned so that the wavelength difference between the pump and the Stokes beams is closer, and thus lower wavenumbers (e.g., down to 200–400 cm^{-1}) can be approached.

The third point to be considered is the mode of light collection. An SRS microscope is often constructed in the transmission mode for biological studies, while the reflection mode is often preferred in materials science to examine material surfaces. For example, epi-detection was demonstrated recently to image the surface of non-transparent samples.[58] In another report, a ring-shaped detector was used to collect the majority of backward emitted photons to image highly scattering samples in the reflection

mode.[83] Moreover, it should be noted that, when pump loss is detected and extracted into the SRS signal, it may suffer from the process of absorption. When strong absorption occurs, the incident pump beam could be severely attenuated, resulting in poor detectability for the desired Raman scattering events. Hence, it is not ideal to apply SRS to materials with strong optical absorption to the pump or the Stokes beams. Instead, as the wavelength of the most commonly used Stokes beam is longer than 1,000 nm, where fewer materials have high extinction coefficients, detecting Stokes gain can be a good solution to the attenuation of the pump beam.

Besides these points, miniaturization and mobilization of an SRS microscope are also important for material sciences, particularly for field studies. Liao et al.[84] developed a background-free and fiber-delivered handheld SRS microscope for *in situ* chemical imaging, where the use of optical fibers enhances the mobility of SRS microscopes. Two ultrafast pulses were temporally separated and propagated in the fiber, then overlapped on the sample. Multiple applications of the handheld SRS microscope were demonstrated, such as imaging bacteria (Figure 9A). The handheld SRS imaging system improves the mobility of SRS and may enable *in situ* compositional analysis for applications in materials science in the future.[84] To reliably use SRS outside the lab, SRS can use lasers with fixed wavenumbers instead of a tunable one. In this way, the instrument will have lower costs, better portability, and better reliability, but the wavenumbers of Stokes and pump lasers need to be pre-set for a specific task.

2) Advancement of instrumentation for enhancing the detection sensitivity and spatial resolution.

Higher spatial resolution and detection sensitivity are always desired for scientific imaging. The synergy between SRS and SERS/TERS can further promote the detection sensitivity down to single-molecule level. SERS requires the target to be adsorbed on rough metal surfaces or nanoparticles and, with the surface plasmon enhancement effect, combination of SRS and SERS can become a fast hyperspectral microscopy with single-molecule sensitivity. Monfared et al.[85] reported a successful combination of SRS and SERS. An enhancement in the SRS signal of ∼12 orders of magnitude is achieved, comparable with that of SERS (Figure 9B). This approach generates a coherent stimulated signal of microwatt intensities, which significantly improves the chemical resolution. Zong et al.[61] demonstrated PESRS microscopy and realized single-molecule detection sensitivity. The SRS spectra show the existence of single-molecule adenine on an Au nanoparticle-SiO_2 substrate, and the distribution of adenine can be depicted using SRS images through background subtraction and a denoising algorithm (Figure 9C). Without PESRS, single-molecule adenine cannot be detected with SRS.

The drawback in SERS is its low spatial resolution. It also highly relies on the specific metal substrates. By replacing the metal substrate in SERS with SPM tips, TERS can be used to study samples on most substrates with much higher spatial resolution. Therefore, the combination of SRS and TERS can realize fast imaging with both chemical and topography information. Rajapaksa and Kumar Wickramasinghe[4] developed a tip-enhanced SRS system by creating a vibration-induced force interaction between tips and samples, and by probing the force with AFM, spectroscopy and microscopy on clusters of molecules have been performed. A nanometer-level resolution is realized with a clean background (Figures 9D and 9E).[4,86]

Besides resolution and sensitivity, imaging quality is also critical. SRS images often suffer from a low SNR due to light absorption and scattering, and it is critical to
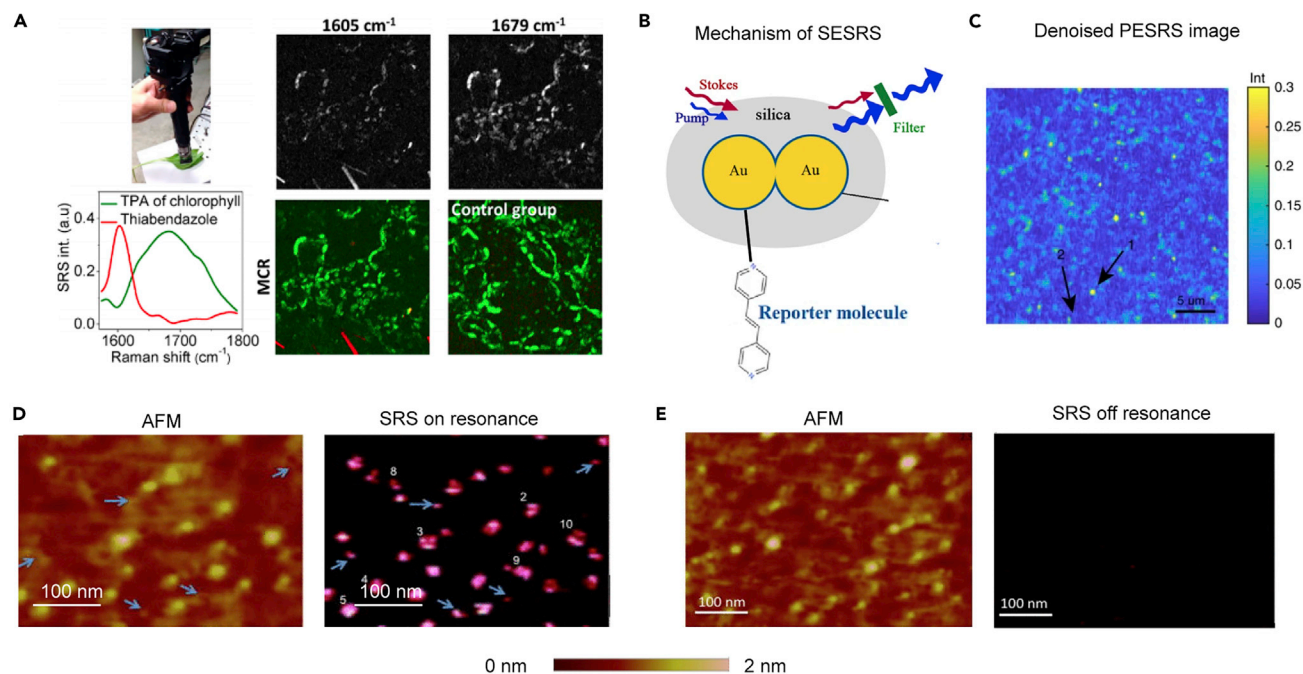
Figure 9. Advances of SRS instrumentation for materials sciences

(A) The image of a handheld microscope and its application in imaging bacteria.[84]

(B) A schematic depiction of a gold/silica nanoprobe used in the continuous-wave SESRS experiment.[85]

(C) The denoised PESRS image of adenine is interpreted from its 733 cm^{-1} peak. Adenine was adsorbed on an Au NPs-SiO$_2$ substrate. The image area is 30 × 30 μm.[61]

(D and E) Topography (left) and Raman images (right) of Coomassie brilliant blue G250 dye molecules on the glass when on-resonance (D) and off-resonance (E). Scale bars, 100 nm.[4]

enhance SNR to acquire better images. Moreover, high-throughput, automatic, and simultaneous analyses on acquired images are important, such as distinguishing target and image segmentation. Toward this goal, machine learning can be a useful tool for SRS imaging. Manifold et al.[87] used a U-Net convolutional neural network to significantly improve the SNR of SRS images. They showed that the algorithm can apply to images acquired at different magnifications, imaging powers, depths, and geometries. Potma and colleagues[88] developed and discussed a methodology for the batch-level analysis of SRS image datasets. They used a training set to determine chemically meaningful reference spectra, followed by a random forest classifier to rapidly classify RS stacks in terms of the pre-determined basis set. The overall procedure allows a rapid quantitative analysis of large SRS datasets, enabling a direct comparison among samples using a single set of reference spectra.

3) Future research topics in materials science.

Over the past decade, the technical developments of SRS microscopy have empowered it to be a versatile tool in imaging applications. Compared with conventional characterization methods, such as X-ray crystallography and electron microscopy, SRS microscopy supplements an indispensable view through the perspective of chemical bonds. Moreover, it can capture the dynamic material phenomena to answer critical questions in the field, such as the transient transport of chemical species. For example, Nafion film is a critical component in proton exchange membrane fuel cells, but it often has problems, such as cation transpassing and water flooding.[89] SRS microscopy could reveal the process of how water molecules transport

in Nafion films and how defects assist protons and other cations to migrate inside the film, which can help design better proton exchange membranes for fuel cells. MOFs have wide applications in gas adsorption, gas storage, proton transportation, and catalysts. SRS may reveal how different chemicals (e.g., gases, protons) diffuse inside MOFs and show underlying transport mechanisms.

Microscopy with broadband spectroscopy is also attractive for materials science since it can obtain critical spectroscopic information to understand dynamic changes at the level of molecular bonding. Spectroscopic information is viable by the tuning of the wavelength of a narrowband laser or by directly using a broadband femtosecond laser.[90] This can have a myriad of potential applications in materials science. For example, the highly concentrated electrolyte, such as solvent-in-salt electrolyte, which usually has a solvation sheath, has been proved to significantly expand the electrochemical windows of electrolytes and form high-quality solid electrolyte interphase (SEI) for lithium metal anodes.[91] Broadband SRS imaging can be used *in situ* to study how the solvation sheath changes upon concentration polarization under an applied current. SRS with rich spectroscopic information also has a great potential in catalysis studies as it can detect intermittent products, capture the dynamic diffusion of reactants and products in solution, identify active sites on catalysts, and study the catalytic reaction mechanisms.

As a far-field imaging platform, SRS is compatible with other near-field amplification methods. The coalition of SRS with resonance or pre-resonance Raman has demonstrated its power.[92,93] Furthermore, SRS may be coupled to other spectroscopy or imaging approaches, such as AFM,[94] photothermal microscopy,[95] or polarized light microscopy, to extend the functionality of Raman imaging and obtain additional information. For example, by combining with an AFM, an SRS microscope may be capable of mapping the stress distribution inside graphene, since stress causes Raman shifts. This can potentially unveil the rupture mechanism of graphene.

The fast imaging speed of an SRS microscope indicates that a large quantity of data will be generated in experiments, so high-throughput data analysis is essential to extracting useful information from SRS images in a fast and accurate fashion. To speed up data collection, Zhang et al.[65] developed a 32-channel multiplex SRS flow cytometry technique, which can measure the chemical contents of a single particle at a speed of 5 µs per Raman spectrum. To speed up data processing, Orringer et al.[96] demonstrated a supervised machine learning approach to effectively identify brain tumors in SRS images.

In summary, with evolving advances in instrumentation and incorporation of data sciences, we believe that SRS microscopy will find various applications in imaging phenomena in materials science. The high-speed, high-sensitivity imaging will open new portals to a broad range of important questions in materials science, which cannot only advance fundamental knowledge but also provide guidance for designing materials and devices with high performance. It will have a significant impact on broad material and energy communities.

AUTHOR CONTRIBUTIONS

Y.Y. and W.M. proposed and supervised the work. Q.C. and Y.M. wrote the paper. All authors have discussed the results and revised the draft.

DECLARATION OF INTERESTS

The authors declare no competing interests.

REFERENCES

1. Tierie, G. (1932). Cornelis Drebbel, H. J. Paris at Amsterdam, Vol. 3.

2. Wood, K.N., Kazyak, E., Chadwick, A.F., Chen, K.-H., Zhang, J.-G., Thornton, K., and Dasgupta, N.P. (2016). Dendrites and pits: untangling the complex behavior of lithium metal anodes through *operando* video microscopy. ACS Cent. Sci. *2*, 790–801.

3. Li, S., Chen, Y.-M., Liang, W., Shao, Y., Liu, K., Nikolov, Z., and Zhu, Y. (2018). A superionic conductive, electrochemically stable dual-salt polymer electrolyte. Joule *2*, 1838–1856.

4. Rajapaksa, I., and Kumar Wickramasinghe, H. (2011). Raman spectroscopy and microscopy based on mechanical force detection. Appl. Phys. Lett. *99*, 161103.

5. Lou, S., Liu, Q., Zhang, F., Liu, Q., Yu, Z., Mu, T., Zhao, Y., Borovilas, J., Chen, Y., and Ge, M. (2020). Insights into interfacial effect and local lithium-ion transport in polycrystalline cathodes of solid-state batteries. Nat. Commun. *11*, 5700.

6. Amenabar, I., Poly, S., Goikoetxea, M., Nuansing, W., Lasch, P., and Hillenbrand, R. (2017). Hyperspectral infrared nanoimaging of organic samples based on Fourier transform infrared nanospectroscopy. Nat. Commun. *8*, 14402.

7. Ilchenko, O., Pilgun, Y., Kutsyk, A., Bachmann, F., Slipets, R., Todeschini, M., Okeyo, P.O., Poulsen, H.F., and Boisen, A. (2019). Fast and quantitative 2D and 3D orientation mapping using Raman microscopy. Nat. Commun. *10*, 5555.

8. Li, Y., Li, Y., Pei, A., Yan, K., Sun, Y., Wu, C.-L., Joubert, L.-M., Chin, R., Koh, A.L., and Yu, Y. (2017). Atomic structure of sensitive battery materials and interfaces revealed by cryo-electron microscopy. Science *358*, 506–510.

9. Wang, X., Pawar, G., Li, Y., Ren, X., Zhang, M., Lu, B., Banerjee, A., Liu, P., Dufek, E.J., and Zhang, J.-G. (2020). Glassy Li metal anode for high-performance rechargeable Li batteries. Nat. Mater. *19*, 1339–1345.

10. Böckmann, H., Gawinkowski, S., Waluk, J., Raschke, M.B., Wolf, M., and Kumagai, T. (2018). Near-field enhanced photochemistry of single molecules in a scanning tunneling microscope junction. Nano Lett. *18*, 152–157.

11. Liu, S.-W., Wang, H.-P., Xu, Q., Ma, T.-B., Yu, G., Zhang, C., Geng, D., Yu, Z., Zhang, S., and Wang, W. (2017). Robust microscale superlubricity under high contact pressure enabled by graphene-coated microsphere. Nat. Commun. *8*, 14029.

12. Yunus, S., Delcorte, A., Poleunis, C., Bertrand, P., Bolognesi, A., and Botta, C. (2007). A route to self-organized honeycomb microstructured polystyrene films and their chemical characterization by ToF-SIMS imaging. Adv. Funct. Mater. *17*, 1079–1084.

13. Forse, A.C., Griffin, J.M., Merlet, C., Carretero-Gonzalez, J., Raji, A.-R.O., Trease, N.M., and Grey, C.P. (2017). Direct observation of ion dynamics in supercapacitor electrodes using in situ diffusion NMR spectroscopy. Nat. Energy *2*, 16216.

14. Mannanov, A.A., Bruevich, V.V., Feldman, E.V., Trukhanov, V.A., Pshenichnikov, M.S., and Paraschuk, D.Y. (2018). Real-time tracking of polymer crystallization dynamics in organic bulk heterojunctions by Raman microscopy. J. Phys. Chem. C *122*, 19289–19297.

15. Reyes-Montero, A., Rubio-Marcos, F., Pardo, L., Del Campo, A., López-Juárez, R., and Villafuerte-Castrejón, M.-E. (2018). Electric field effect on the microstructure and properties of $Ba_{0.9}Ca_{0.1}Ti_{0.9}Zr_{0.1}O_3$ (BCTZ) lead-free ceramics. J. Mater. Chem. A *6*, 5419–5429.

16. Ferrari, A.C., Meyer, J., Scardaci, V., Casiraghi, C., Lazzeri, M., Mauri, F., Piscanec, S., Jiang, D., Novoselov, K., and Roth, S. (2006). Raman spectrum of graphene and graphene layers. Phys. Rev. Lett. *97*, 187401.

17. Sharikova, A., Foraida, Z.I., Sfakis, L., Peerzada, L., Larsen, M., Castracane, J., and Khmaladze, A. (2020). Characterization of nanofibers for tissue engineering: chemical mapping by confocal Raman microscopy. Spectrochim. Acta A Mol. Biomol. Spectrosc. *227*, 117670.

18. Ao, J., Feng, Y., Wu, S., Wang, T., Ling, J., Zhang, L., and Ji, M. (2020). Rapid, 3D chemical profiling of individual atmospheric aerosols with stimulated Raman scattering microscopy. Small Methods *4*, 1900600.

19. Houle, M.A., Burruss, R.C., Ridsdale, A., Moffatt, D.J., Légaré, F., and Stolow, A. (2017). Rapid 3D chemical-specific imaging of minerals using stimulated Raman scattering microscopy. J. Raman Spectrosc. *48*, 726–735.

20. Liu, K.-L., Kubarev, A.V., Van Loon, J., Uji-i, H., De Vos, D.E., Hofkens, J., and Roeffaers, M.B. (2014). Rationalizing inter- and intracrystal heterogeneities in dealuminated acid mordenite zeolites by stimulated Raman scattering microscopy correlated with super-resolution fluorescence microscopy. ACS Nano *8*, 12650–12659.

21. Ling, J., Miao, X., Sun, Y., Feng, Y., Zhang, L., Sun, Z., and Ji, M. (2019). Vibrational imaging and quantification of two-dimensional hexagonal boron nitride with stimulated Raman scattering. ACS Nano *13*, 14033–14040.

22. Cheng, Q., Wei, L., Liu, Z., Ni, N., Sang, Z., Zhu, B., Xu, W., Chen, M., Miao, Y., and Chen, L.-Q. (2018). Operando and three-dimensional visualization of anion depletion and lithium growth by stimulated Raman scattering microscopy. Nat. Commun. *9*, 2942.

23. Wei, L., Chen, Z., Shi, L., Long, R., Anzalone, A.V., Zhang, L., Hu, F., Yuste, R., Cornish, V.W., and Min, W. (2017). Super-multiplex vibrational imaging. Nature *544*, 465–470.

24. Xiong, H.Q., Lee, J.K., Zare, R.N., and Min, W. (2020). Strong electric field observed at the interface of aqueous microdroplets. J. Phys. Chem. Lett. *11*, 7423–7428.

25. Li, H., Cheng, Y., Tang, H., Bi, Y., Chen, Y., Yang, G., Guo, S., Tian, S., Liao, J., and Lv, X. (2020). Imaging chemical kinetics of radical polymerization with an ultrafast coherent Raman microscope. Adv. Sci. 1903644.

26. Sarri, B., Canonge, R., Audier, X., Lavastre, V., Pénarier, G., Alie, J., and Rigneault, H. (2019). Discriminating polymorph distributions in pharmaceutical tablets using stimulated Raman scattering microscopy. J. Raman Spectrosc. *50*, 1896–1904.

27. Zada, L., Leslie, H.A., Vethaak, A.D., Tinnevelt, G.H., Jansen, J.J., de Boer, J.F., and Ariese, F. (2018). Fast microplastics identification with stimulated Raman scattering microscopy. J. Raman Spectrosc. *49*, 1136–1144.

28. Freudiger, C.W., Min, W., Saar, B.G., Lu, S., Holtom, G.R., He, C.W., Tsai, J.C., Kang, J.X., and Xie, X.S. (2008). Label-free biomedical imaging with high sensitivity by stimulated Raman scattering. Science *322*, 1857–1861.

29. Nie, S.M., and Emery, S.R. (1997). Probing single molecules and single nanoparticles by surface-enhanced Raman scattering. Science *275*, 1102–1106.

30. Ozeki, Y., Umemura, W., Otsuka, Y., Satoh, S., Hashimoto, H., Sumimura, K., Nishizawa, N., Fukui, K., and Itoh, K. (2012). High-speed molecular spectral imaging of tissue with stimulated Raman scattering. Nat. Photon. *6*, 845–851.

31. Camp, C.H., Jr., and Cicerone, M.T. (2015). Chemically sensitive bioimaging with coherent Raman scattering. Nat. Photon. *9*, 295.

32. Hu, F., Shi, L., and Min, W. (2019). Biological imaging of chemical bonds by stimulated Raman scattering microscopy. Nat. Methods *16*, 830–842.

33. Cheng, X., Xian, F., Hu, Z., Wang, C., Du, X., Zhang, H., Chen, S., Dong, S., and Cui, G. (2019). Fluorescence probing of active lithium distribution in lithium metal anodes. Angew. Chem. *131*, 5997–6001.

34. Shi, L., Zheng, C., Shen, Y., Chen, Z., Silveira, E.S., Zhang, L., Wei, M., Liu, C., de Sena-Tomas, C., Targoff, K., et al. (2018). Optical imaging of metabolic dynamics in animals. Nat. Commun. *9*, 2995.

35. Hu, F., Chen, Z., Zhang, L., Shen, Y., Wei, L., and Min, W. (2015). Vibrational imaging of glucose uptake activity in live cells and tissues by stimulated Raman scattering. Angew. Chem. Int. Ed. *54*, 9821–9825.

36. Long, R., Zhang, L., Shi, L., Shen, Y., Hu, F., Zeng, C., and Min, W. (2018). Two-color vibrational imaging of glucose metabolism using stimulated Raman scattering. Chem. Commun. *54*, 152–155.

37. Zhang, L., Shi, L., Shen, Y., Miao, Y., Wei, M., Qian, N., Liu, Y., and Min, W. (2019). Spectral tracing of deuterium for imaging glucose metabolism. Nat. Biomed. Eng. *3*, 402–413.

38. Shen, Y., Zhao, Z., Zhang, L., Shi, L., Shahriar, S., Chan, R.B., Di Paolo, G., and Min, W. (2017). Metabolic activity induces membrane phase separation in endoplasmic reticulum. Proc. Natl. Acad. Sci. U S A *114*, 13394–13399.

39. Wakisaka, Y., Suzuki, Y., Iwata, O., Nakashima, A., Ito, T., Hirose, M., Domon, R., Sugawara, M., Tsumura, N., Watarai, H., et al. (2016). Probing the metabolic heterogeneity of live *Euglena gracilis* with stimulated Raman scattering microscopy. Nat. Microbiol. *1*, 16124.

40. Schiessl, K.T., Hu, F.H., Jo, J., Nazia, S.Z., Wang, B., Price-Whelan, A., Min, W., and Dietrich, L.E.P. (2019). Phenazine production promotes antibiotic tolerance and metabolic heterogeneity in *Pseudomonas aeruginosa* biofilms. Nat. Commun. *10*, 762.

41. Fleury, G., Steele, J.A., Gerber, I.C., Jolibois, F., Puech, P., Muraoka, K., Keoh, S.H., Chaikittisilp, W., Okubo, T., and Roeffaers, M.B. (2018). Resolving the framework position of organic structure-directing agents in hierarchical zeolites via polarized stimulated Raman scattering. J. Phys. Chem. Lett. *9*, 1778–1782.

42. Miao, X., Zhang, G., Wang, F., Yan, H., and Ji, M. (2018). Layer-dependent ultrafast carrier and coherent phonon dynamics in black phosphorus. Nano Lett. *18*, 3053–3059.

43. Eom, C.J., and Suntivich, J. (2019). In situ stimulated Raman spectroscopy reveals the phosphate network in the amorphous cobalt oxide catalyst and its role in the catalyst formation. J. Phys. Chem. C *123*, 29284–29290.

44. Li, Z., Li, H., Fang, W., Wang, S., Sun, C., Li, Z., and Men, Z. (2015). Pre-resonance-stimulated Raman scattering for water bilayer structure on laser-induced plasma bubble surface. Opt. Lett. *40*, 3253–3255.

45. Figueroa, B., Nguyen, T., Sotthivirat, S., Xu, W., Rhodes, T., Lamm, M.S., Smith, R.L., John, C.T., Su, Y., and Fu, D. (2019). Detecting and quantifying microscale chemical reactions in pharmaceutical tablets by stimulated Raman scattering microscopy. Anal. Chem. *91*, 6894–6901.

46. Larkin, P. (2011). Infrared and Raman Spectroscopy: Principles and Spectral Interpretation (Elsevier).

47. Butler, H.J., Ashton, L., Bird, B., Cinque, G., Curtis, K., Dorney, J., Esmonde-White, K., Fullwood, N.J., Gardner, B., Martin-Hirsch, P.L., et al. (2016). Using Raman spectroscopy to characterize biological materials. Nat. Protoc. *11*, 664–687.

48. Schmid, T., Opilik, L., Blum, C., and Zenobi, R. (2013). Nanoscale chemical imaging using tip-enhanced Raman spectroscopy: a critical review. Angew. Chem. Int. Ed. *52*, 5940–5954.

49. Cheng, J.X., and Xie, X.S. (2015). Vibrational spectroscopic imaging of living systems: an emerging platform for biology and medicine. Science *350*, aaa8870.

50. Asher, S.A. (1988). UV resonance Raman studies of molecular-structure and dynamics—applications in physical and biophysical chemistry. Annu. Rev. Phys. Chem. *39*, 537–588.

51. Schellenberg, P., Johnson, E., Esposito, A.P., Reid, P.J., and Parson, W.W. (2001). Resonance Raman scattering by the green fluorescent protein and an analogue of its chromophore. J. Phys. Chem. B *105*, 5316–5322.

52. Wei, L., Hu, F., Shen, Y., Chen, Z., Yu, Y., Lin, C.C., Wang, M.C., and Min, W. (2014). Live-cell imaging of alkyne-tagged small biomolecules by stimulated Raman scattering. Nat. Methods *11*, 410–412.

53. Zhao, Z., Shen, Y., Hu, F., and Min, W. (2017). Applications of vibrational tags in biological imaging by Raman microscopy. Analyst *142*, 4018–4029.

54. Ji, M., Arbel, M., Zhang, L., Freudiger, C.W., Hou, S.S., Lin, D., Yang, X., Bacskai, B.J., and Xie, X.S. (2018). Label-free imaging of amyloid plaques in Alzheimer's disease with stimulated Raman scattering microscopy. Sci. Adv. *4*, eaat7715.

55. Fu, D., Yang, W., and Xie, X.S. (2017). Label-free imaging of neurotransmitter acetylcholine at neuromuscular junctions with stimulated Raman scattering. J. Am. Chem. Soc. *139*, 583–586.

56. Fu, D., Yu, Y., Folick, A., Currie, E., Farese, R.V., Jr., Tsai, T.H., Xie, X.S., and Wang, M.C. (2014). *In vivo* metabolic fingerprinting of neutral lipids with hyperspectral stimulated Raman scattering microscopy. J. Am. Chem. Soc. *136*, 8820–8828.

57. Asai, T., Liu, H., Ozeki, Y., Sato, S., Hayashi, T., and Nakamura, H. (2019). Imaging of cellular uptake of boron cluster compound by stimulated Raman scattering microscopy. Appl. Phys. Express *12*, 112004.

58. Saar, B.G., Freudiger, C.W., Reichman, J., Stanley, C.M., Holtom, G.R., and Xie, X.S. (2010). Video-rate molecular imaging in vivo with stimulated Raman scattering. Science *330*, 1368–1370.

59. Denk, W., Strickler, J.H., and Webb, W.W. (1990). Two-photon laser scanning fluorescence microscopy. Science *248*, 73–76.

60. Xiong, H.Q., Shi, L.X., Wei, L., Shen, Y.H., Long, R., Zhao, Z.L., and Min, W. (2019). Stimulated Raman excited fluorescence spectroscopy and imaging. Nat. Photon. *13*, 412–417.

61. Zong, C., Premasiri, R., Lin, H., Huang, Y., Zhang, C., Yang, C., Ren, B., Ziegler, L.D., and Cheng, J.X. (2019). Plasmon-enhanced stimulated Raman scattering microscopy with single-molecule detection sensitivity. Nat. Commun. *10*, 5318.

62. Jundt, D.H. (1997). Temperature-dependent Sellmeier equation for the index of refraction, $n(e)$, in congruent lithium niobate. Opt. Lett. *22*, 1553–1555.

63. Fu, D., Holtom, G., Freudiger, C., Zhang, X., and Xie, X.S. (2013). Hyperspectral imaging with stimulated Raman scattering by chirped femtosecond lasers. J. Phys. Chem. B *117*, 4634–4640.

64. Rock, W., Bonn, M., and Parekh, S.H. (2013). Near shot-noise limited hyperspectral stimulated Raman scattering spectroscopy using low energy lasers and a fast CMOS array. Opt. Express *21*, 15113–15120.

65. Zhang, C., Huang, K.-C., Rajwa, B., Li, J., Yang, S., Lin, H., Liao, C.-s., Eakins, G., Kuang, S., and Patsekin, V. (2017). Stimulated Raman scattering flow cytometry for label-free single-particle analysis. Optica *4*, 103–109.

66. Bi, Y., Yang, C., Chen, Y., Yan, S., Yang, G., Wu, Y., Zhang, G., and Wang, P. (2018). Near-resonance enhanced label-free stimulated Raman scattering microscopy with spatial resolution near 130 nm. Light Sci. Appl. *7*, 81.

67. Silva, W.R., Graefe, C.T., and Frontiera, R.R. (2015). Toward label-free super-resolution microscopy. ACS Photon. *3*, 79–86.

68. Wei, M., Shi, L.Y., Shen, Y.H., Zhao, Z.L., Guzman, A., Kaufman, L.J., Wei, L., and Min, W. (2019). Volumetric chemical imaging by clearing-enhanced stimulated Raman scattering microscopy. Proc. Natl. Acad. Sci. U S A *116*, 6608–6617.

69. Chen, X., Zhang, C., Lin, P., Huang, K.C., Liang, J., Tian, J., and Cheng, J.X. (2017). Volumetric chemical imaging by stimulated Raman projection microscopy and tomography. Nat. Commun. *8*, 15117.

70. Zhang, L., Shen, S., Liu, Z., and Ji, M. (2017). Label-free, quantitative imaging of MoS_2-nanosheets in live cells with simultaneous stimulated Raman scattering and transient absorption microscopy. Adv. Biosyst. *1*, 1700013.

71. Přech, J., Pizarro, P., Serrano, D., and Čejka, J. (2018). From 3D to 2D zeolite catalytic materials. Chem. Soc. Rev. *47*, 8263–8306.

72. Laptenok, S.P., Martin, C., Genchi, L., Duarte, C.M., and Liberale, C. (2020). Stimulated Raman microspectroscopy as a new method to classify microfibers from environmental samples. Environ. Pollut. *267*, 115640.

73. Lee, J.K., Banerjee, S., Nam, H.G., and Zare, R.N. (2015). Acceleration of reaction in charged microdroplets. Q. Rev. Biophys. *48*, 437–444.

74. Wei, Z.W., Li, Y.J., Cooks, R.G., and Yan, X. (2020). Accelerated reaction kinetics in microdroplets: overview and recent developments. Annu. Rev. Phys. Chem. *71*, 31–51.

75. Bai, P., Li, J., Brushett, F.R., and Bazant, M.Z. (2016). Transition of lithium growth mechanisms in liquid electrolytes. Energy Environ. Sci. *9*, 3221–3229.

76. Perez, E.V., Balkus, K.J., Jr., Ferraris, J.P., and Musselman, I.H. (2009). Mixed-matrix membranes containing MOF-5 for gas separations. J. Membr. Sci. *328*, 165–173.

77. Chmelik, C., Hibbe, F., Tzoulaki, D., Heinke, L., Caro, J., Li, J., and Kärger, J. (2010). Exploring the nature of surface barriers on MOF Zn(tbip) by applying IR microscopy in high temporal and spatial resolution. Micropor. Mesopor. Mater. *129*, 340–344.

78. Ma, M., Gross, A., Zacher, D., Pinto, A., Noei, H., Wang, Y., Fischer, R.A., and Metzler-Nolte, N. (2011). Use of confocal fluorescence microscopy to compare different methods of modifying metal–organic framework (MOF) crystals with dyes. CrystEngComm *13*, 2828–2832.

79. van Haasterecht, L., Zada, L., Schmidt, R.W., de Bakker, E., Barbé, E., Leslie, H.A., Vethaak, A.D., Gibbs, S., de Boer, J.F., and Niessen, F.B. (2020). Label-free stimulated Raman scattering imaging reveals silicone breast implant material in tissue. J. Biophotonics *13*, e201960197.

80. Chagnes, A., Carré, B., Willmann, P., and Lemordant, D. (2002). Modeling viscosity and conductivity of lithium salts in γ-butyrolactone. J. Power Sourc. *109*, 203–213.

81. Kondo, K., Sano, M., Hiwara, A., Omi, T., Fujita, M., Kuwae, A., Iida, M., Mogi, K., and Yokoyama, H. (2000). Conductivity and solvation of Li$^+$ ions of LiPF$_6$ in propylene carbonate solutions. J. Phys. Chem. B *104*, 5040–5044.

82. Briggs, A.G., Hampson, N.A., and Marshall, A. (1974). Concentrated potassium zincate solutions studied using laser Raman spectroscopy and potentiometry. J. Chem. Soc. Faraday Trans. *70*, 1978–1990.

83. Slipchenko, M.N., Chen, H.T., Ely, D.R., Jung, Y., Carvajal, M.T., and Cheng, J.X. (2010). Vibrational imaging of tablets by epi-detected stimulated Raman scattering microscopy. Analyst *135*, 2613–2619.

84. Liao, C.-S., Wang, P., Huang, C.Y., Lin, P., Eakins, G., Bentley, R.T., Liang, R., and Cheng, J.-X. (2017). *In vivo* and *in situ* spectroscopic imaging by a handheld stimulated Raman scattering microscope. ACS Photon. *5*, 947–954.

85. Monfared, Y.E., Shaffer, T.M., Gambhir, S.S., and Hewitt, K.C. (2019). Continuous-wave coherent Raman spectroscopy via plasmonic enhancement. Sci. Rep. *9*, 12092.

86. Tamma, V.A., Huang, F., Nowak, D., and Wickramasinghe, H.K. (2016). Stimulated Raman spectroscopy and nanoscopy of molecules using near field photon induced forces without resonant electronic enhancement gain. Appl. Phys. Lett. *108*, 233107.

87. Manifold, B., Thomas, E., Francis, A.T., Hill, A.H., and Fu, D. (2019). Denoising of stimulated Raman scattering microscopy images via deep learning. Biomed. Opt. Express *10*, 3860–3874.

88. Alfonso-García, A., Paugh, J., Farid, M., Garg, S., Jester, J., and Potma, E. (2017). A machine learning framework to analyze hyperspectral stimulated Raman scattering microscopy images of expressed human meibum. J. Raman Spectrosc. *48*, 803–812.

89. Sukkar, T., and Skyllas-Kazacos, M. (2003). Water transfer behaviour across cation exchange membranes in the vanadium redox battery. J. Membr. Sci. *222*, 235–247.

90. Freudiger, C.W., Min, W., Holtom, G.R., Xu, B., Dantus, M., and Xie, X.S. (2011). Highly specific label-free molecular imaging with spectrally tailored excitation-stimulated Raman scattering (STE-SRS) microscopy. Nat. Photon. *5*, 103–109.

91. Suo, L., Borodin, O., Gao, T., Olguin, M., Ho, J., Fan, X., Luo, C., Wang, C., and Xu, K. (2015). "Water-in-salt" electrolyte enables high-voltage aqueous lithium-ion chemistries. Science *350*, 938–943.

92. Wei, L., and Min, W. (2018). Electronic preresonance stimulated Raman scattering microscopy. J. Phys. Chem. Lett. *9*, 4294–4301.

93. Shi, L., Xiong, H., Shen, Y., Long, R., Wei, L., and Min, W. (2018). Electronic resonant stimulated Raman scattering micro-spectroscopy. J. Phys. Chem. B *122*, 9218–9224.

94. Dazzi, A., and Prater, C.B. (2017). AFM-IR: technology and applications in nanoscale infrared spectroscopy and chemical imaging. Chem. Rev. *117*, 5146–5173.

95. Zhang, D.L., Li, C., Zhang, C., Slipchenko, M.N., Eakins, G., and Cheng, J.X. (2016). Depth-resolved mid-infrared photothermal imaging of living cells and organisms with submicrometer spatial resolution. Sci. Adv. *2*, e1600521.

96. Orringer, D.A., Pandian, B., Niknafs, Y.S., Hollon, T.C., Boyle, J., Lewis, S., Garrard, M., Hervey-Jumper, S.L., Garton, H.J., and Maher, C.O. (2017). Rapid intraoperative histology of unprocessed surgical specimens via fibre-laser-based stimulated Raman scattering microscopy. Nat. Biomed. Eng. *1*, 0027.